50th AIAA Aerospace Sciences Meeting including the New Horizons Forum and Aerospace Exposition
09 - 12 January 2012, Nashville, Tennessee

AIAA 2012-0282

Hypersonic Boundary-Layer Transition Experiments in the Boeing/AFOSR Mach-6 Quiet Tunnel

Christopher A. C. Ward*, Bradley M. Wheaton*, Amanda Chou*,
Dennis C. Berridge*, Laura E. Letterman*,
Ryan P. K. Luersen*, and Steven P. Schneider†
School of Aeronautics and Astronautics
Purdue University
West Lafayette, IN 47907-1282

This paper reports progress from six different projects studying hypersonic boundary-layer transition. Efforts to measure instabilities in the wake of an isolated roughness element in the laminar nozzle-wall boundary layer of the BAM6QT are on-going. A new set of instabilities have been measured when the roughness is at a height that causes incipient transition within the measurement range. The second project tested a method of calibrating temperature-sensitive paints using Schmidt-Boelter heat transfer gauges. A 7-deg half-angle cone was tested at 0-deg angle of attack and the heat transfer compared well with theory. A forward-facing cavity was used to identify the critical depth where self-sustaining oscillations begin. This was found to be about 1.2 cavity diameters. A shock tube is being constructed at Purdue to calibrate PCB-132 sensors. The tube will create clean, weak shocks of a magnitude similar to a second-mode wave in a wind tunnel, allowing accurate calibrations for instability measurements. A flared cone was tested in the BAM6QT, and showed natural transition under fully quiet flow. The streamwise vortices visible on the surface of the cone were found to be body fixed. A blunt 3-deg half-angle cone was tested with various distributed and isolated roughness elements.

Nomenclature

a	speed of sound	p	pressure (psia)
c_p	specific heat capacity	ρ	density
δ	boundary layer thickness	$\dot{q}$	heat flux
D	diameter	Re	Reynolds number
f	frequency	St	Stanton number
k	roughness height	T	Temperature
h	enthalpy	t	time
H	total enthalpy	u	velocity
L	depth of cavity	μ	viscosity
M	Mach number	x	axial coordinate
N	integrated amplification factor		

*Research Assistant. Student Member, AIAA
†Professor. Associate Fellow, AIAA

Subscripts

0	stagnation condition
∞	freestream condition
k	based on roughness height
i	initial condition
w	wall condition

Superscripts

$'$	fluctuations

Abbreviations

BAM6QT	Boeing/AFOSR Mach-6 Quiet Tunnel
TSP	Temperature-Sensitive Paint
RMS	root mean square
SB	Schmidt-Boelter heat transfer gauge

I. Introduction

A. Hypersonic Boundary-Layer Transition

Hypersonic laminar-to-turbulent transition is important for prediction and control of heat transfer, skin friction, separation and other boundary-layer properties. Vehicles that spend extended periods at hypersonic speeds may be critically affected by uncertainties in transition prediction, depending on their Reynolds numbers. However, the mechanisms leading to transition are still poorly understood, even in low-noise environments.

Boundary-layer transition is a complicated process. Disturbances can be created in the freestream (acoustic radiation or vorticity) or by the vehicular surface (surface roughness or waviness).[1] The disturbances enter the boundary layer through the process of receptivity.[2] Receptivity can be affected by roughness, bluntness, Mach number and other factors. These disturbances grow and may lead to turbulence, depending on the instabilities present in the boundary layer. Empirical or semi-empirical methods can be used to predict the growth of these instabilities and predict transition,[3] but these empirical methods are not necessarily reliable for a wide range of cases. A more basic understanding of the flow physics that causes transition is needed, thereby reducing empiricism.

B. The Boeing/AFOSR Mach-6 Quiet Tunnel

The Boeing/AFOSR Mach-6 Quiet Tunnel (BAM6QT), shown in Figure 1, is the largest operational hypersonic quiet tunnel in the world. The BAM6QT is a Ludwieg tube, consisting of a long driver tube with a converging-diverging nozzle at the downstream end. A Ludwieg tube design was chosen since it can provide high quiet Reynolds numbers while minimizing costs. The tunnel is operated by bringing the driver tube and the test section to the desired stagnation pressure and the downstream end to vacuum, separated by a set of double-burst diaphragms. To run the tunnel the diaphragms are burst, causing a shock wave to travel downstream and an expansion fan to travel upstream. Mach-6 flow is initiated when the expansion fan passes through the nozzle. The expansion fan reflects between the upstream end of the driver tube and the contraction, causing a quasi-static decrease in the stagnation pressure. Therefore, for any given run a range of Reynolds numbers can be tested.

The BAM6QT is capable of maintaining a laminar nozzle-wall boundary layer, thus producing freestream noise levels that are less than 0.05% of the mean. The BAM6QT employs several features to achieve this low noise. A suction slot is present upstream of the throat and removes the boundary layer on the contraction wall, allowing a new undisturbed laminar boundary layer to grow on the nozzle wall. The suction slot is connected to the vacuum tank through a fast valve. The fast valve can be closed to allow a turbulent nozzle-wall boundary layer to develop. The noise levels with a turbulent nozzle-wall boundary layer are on the order of 3%, similar to conventional hypersonic tunnels. The tunnel also features a long nozzle to damp the effect of the Görtler instability, a highly polished throat and nozzle, and high-quality air filters to reduce airborne particulate.

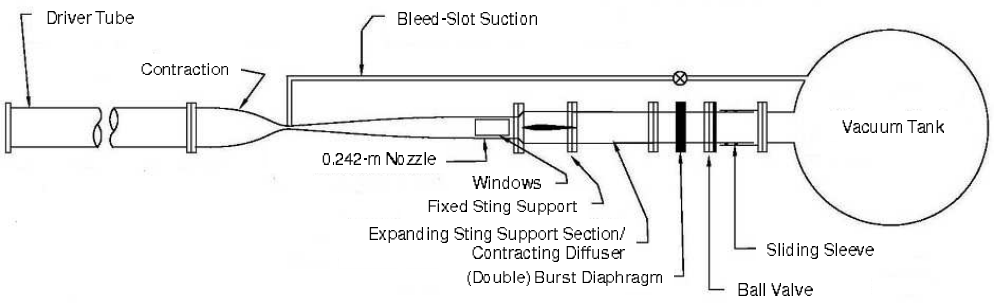

Figure 1. Schematic of Boeing/AFOSR Mach-6 Quiet Tunnel

II. Instability and Transition in the Wake of an Isolated Cylindrical Roughness

A. Measuring Instabilities due to Near-Critical Roughness Elements

To develop improved methods of transition prediction for isolated roughness based on the growth of disturbances in the roughness wake, the underlying instability mechanisms must first be characterized. A cylindrical roughness element has been used to introduce instabilities into the laminar nozzle-wall boundary layer in the BAM6QT.[4–9] Previous work involved characterization of instabilities that occur due to large roughness heights, on the order of the boundary-layer thickness or higher. For a roughness height of 1.2–1.3 times the boundary-layer thickness, an instability was detected with a frequency near 21 kHz.[4,5] The instability was confirmed by direct numerical simulations performed at the University of Minnesota.[8,10] The computations suggested that this instability originated in the separation region upstream of the roughness, a fact later verified with experimental measurements.[7] For this case, transition was observed to occur as close as 20 roughness diameters (D) downstream. It seems likely that this instability occurs for "nearly-effective" trips, or trips of sufficient height to cause transition relatively close to the roughness.

While previous work focused on instabilities due to nearly-effective roughness, the present work explores instabilities due to small, "nearly-critical" roughness elements. Here, nearly-critical roughness elements are defined as trips at or near the minimum height required to induce transition on the nozzle wall within the measurement range available. To detect instabilities, flush-mounted pressure transducers are mounted in the nozzle wall at streamwise locations up to $152.0D$ downstream of the roughness. For these small roughness heights, new instabilities have been detected that occur far downstream of the roughness.

B. Configuration for Surface-Pressure Measurements of Instabilities

A 5.97-mm-diameter micrometer head was used as the cylindrical roughness element, located on the nozzle wall at an axial distance of 1.924 m from the throat. The height k of the roughness can be adjusted from 0.00–24.31 mm with a precision of ± 0.05 mm. For the measurements reported here, the roughness was placed on the tunnel centerplane on the upper wall of the nozzle. An array of Kulite XCQ-062-15A pressure transducers with A screens were placed along the tunnel centerplane in the roughness wake at various streamwise positions. Compared to measuring instabilities with a hot-wire or pitot probe, surface-pressure measurements are advantageous because they are relatively non-intrusive and allow simultaneous acquisition of data at many streamwise locations.

Figure 2 shows a photograph of the apparatus as well as a side-view schematic of the streamwise positions available for pressure-sensor installation with the approximate locations marked by dashes on the line above the schematic. The last section of the nozzle cannot be easily modified so the sensor locations are limited to various inserts. The sensors are placed in any of four locations: (1) near the roughness (not in the

present experiments), (2) in a small circular insert approximately $20D$ downstream of the roughness, (3) in a long insert placed in the slot normally used for probe insertion, (4) along the upper wall of the pipe insert downstream of the nozzle exit. The pipe insert has a 0.242-m inner diameter and is placed immediately downstream of the nozzle exit to extend the location of the last sensor from $93.1D$ to $152.0D$ downstream of the roughness at $p_0 = 90$ psia. The boundary-layer thickness $\delta_{0.995}$ is defined as the height above the wall at which the local streamwise velocity is 99.5% of the freestream value. For a stagnation pressure of $p_0 = 90$ psia, the location of the last sensor is increased from $60\delta_{0.995}$ to $100\delta_{0.995}$ downstream of the roughness when using the pipe insert. Experiments by Casper[11] have verified that the laminar boundary layer extends beyond the nozzle exit along the pipe insert - though with a greater likelihood of intermittent disturbances. These intermittent disturbances were not observed at the relatively low stagnation pressures in the present experiments.

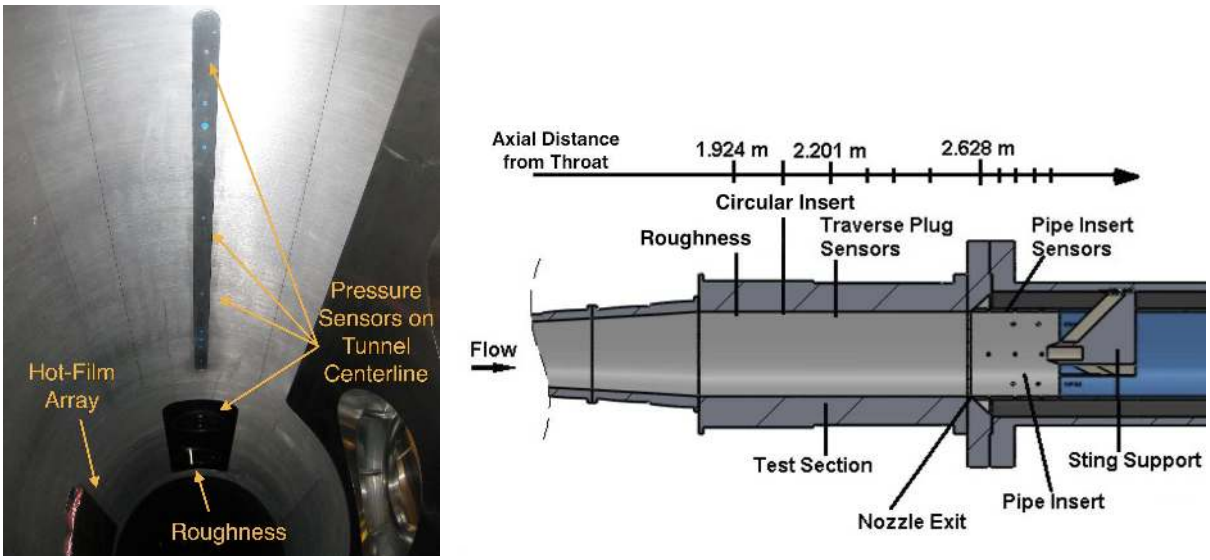

(a) Photograph looking upstream

(b) Side-view schematic

Figure 2. Apparatus for non-intrusive surface-pressure measurements: photograph looking upstream from the exit of the nozzle and side-view schematic of setup.

C. Data Acquisition and Analysis

Probe and sidewall pressure-sensor data were sampled at 500 kHz in Hi-Res mode on a Tektronix DPO7054 Oscilloscope. Hi-Res mode is a method of digital filtering in which the scope acquires data at its maximum sampling frequency of 500 MHz. The scope computes a real-time average over 1,000-point intervals to record an averaged result at the desired sampling frequency of 500 kHz. This mode effectively acts as a low-pass filter to eliminate signal aliasing.

Experimental power spectra were computed using Welch's method to examine the frequency content of the signal. The spectra were computed from 0.1 second samples using Hamming windows with 50% overlap. The window size was 1/40 of the number of points in the 0.1-s sample for a total of 60 windows. Smooth-wall laminar and turbulent spectra were obtained from separate runs with no roughness, using bleed suction to control the state of the nozzle-wall boundary layer. The pressure fluctuations from the roughness wake were nondimensionalized by the calculated freestream pressure at Mach 6.

D. Results

1. *Effect of Roughness Height on Streamwise Pressure Fluctuations*

Surface-pressure power spectra were computed downstream of roughnesses of various heights (k) from 2.79–3.30 mm from several runs during a single tunnel entry (Figure 3). The tests were performed in the BAM6QT during runs with an initial stagnation pressure of 95 psia. All data were analyzed at a stagnation pressure of 88 psia from 1.0-1.1 s into the run. Bleed suction was used to obtain a laminar boundary layer on the nozzle wall. At these conditions, the boundary-layer thickness $\delta_{0.995}$ at the location of the roughness is approximately 7.6 mm. The boundary-layer thickness was calculated using the Harris finite-difference boundary-layer code,[12] assuming a nozzle-wall temperature distribution from a finite-element heat-transfer analysis performed by Skoch.[13] Note that the data in Figure 3 are taken from the same week of experiments. There appears to be some slight variations in the instability amplitudes at certain conditions during repeated runs in different weeks. This will be discussed in Section 2.

The sensors were located along the centerline of the roughness wake at x/D = 46.3, 63.3, 76.1, 93.1, 118.0, 126.5, 135.0, and 143.5. The coordinate x/D represents the axial distance downstream of the roughness nondimensionalized by the roughness diameter D. Typical smooth-wall laminar and turbulent spectra are shown from similar conditions without the roughness present. Possible transition is indicated when the spectrum amplitudes approach the smooth-wall turbulent levels and the peaks in the spectrum broaden and can no longer be distinguished. Prior to transition, the spectral amplitudes may "overshoot" the smooth-wall turbulent levels. This overshoot is consistent with the maximum RMS pressure that has been observed to occur as the flow is transitioning from laminar to turbulent.[14]

At the smallest roughness height of 2.79 mm (Figure 3(a)), the spectra appear laminar and steady until approximately x/D = 118.0 where a peak appears near 23 kHz. The peak broadens and grows in amplitude with downstream distance. This peak appears to be a new instability that has not previously been reported. At the farthest downstream sensor at x/D = 143.5 the fluctuation amplitudes remain lower than those in the turbulent boundary layer.

When the roughness height is increased slightly to 2.92 mm (Figure 3(b)), possible transition occurs within the downstream portion of the measurement range. At x/D = 76.1, a peak can again be seen near 23 kHz. However, at this roughness height a second peak occurs near 50 kHz. It is this second peak that appears to grow to large amplitudes by x/D = 118.0. The amplitudes rise above those of the smooth-wall turbulent boundary layer and by x/D = 143.5 the spectra appears to show broadband turbulent fluctuation levels along with a disappearance of the instability peak. This would seem to indicate that transition has occurred for this case.

In Figure 3(c) showing the k = 3.05 mm case, up to three peaks are seen at 23 kHz, 30 kHz, and 55 kHz. At this higher roughness height, it seems that transition is moving forward as expected. The fluctuation amplitudes first rise above turbulent levels at x/D = 93.1 for this case. When k = 3.18 mm (Figure 3(d)), the peaks appear to be wider than in the k = 3.05 mm case with the amplitudes nearing turbulent levels near x/D = 76.1. At the highest roughness height of 3.30 mm (Figure 3(e)), the fluctuation amplitudes pass turbulent levels near x/D = 63.3.

2. *Repeatability of Pressure Fluctuations for Nearly-Critical Roughness*

The data in Figure 3 were taken during a single week in July 2011. Further tests were performed in October 2011 to determine the repeatability of the instability frequencies and amplitudes for several roughness heights. All runs were performed with an initial stagnation pressure near $p_{0,i}$ = 95 psia and the data were analyzed from 1.0-1.1 s into the run. The stagnation pressure p_0 = 88 psia was the same between the runs. Power spectra along the wake centerline for repeated runs with roughness heights of 2.79, 3.05, and 3.30 mm are shown in Figure 4. Smooth-wall laminar and turbulent spectra are also shown for comparison. Each line color represents a particular location along the roughness wake centerline, and the letter symbols represent a particular run (with the conditions summarized in Table 1). For good repeatability, spectra sharing a particular color should have identical amplitudes. The same sensors were used between the entries, however

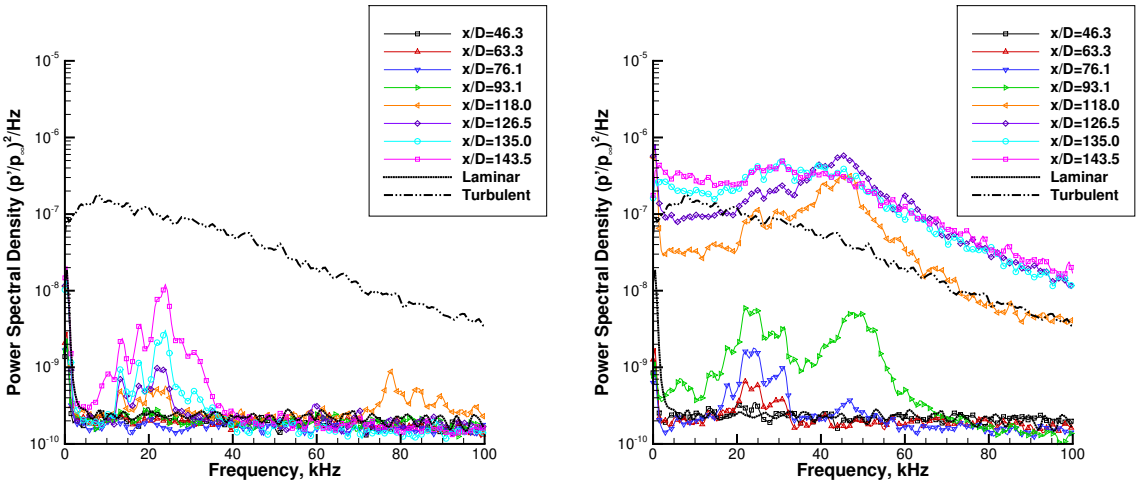

(a) $k = 2.79$ mm

(b) $k = 2.92$ mm

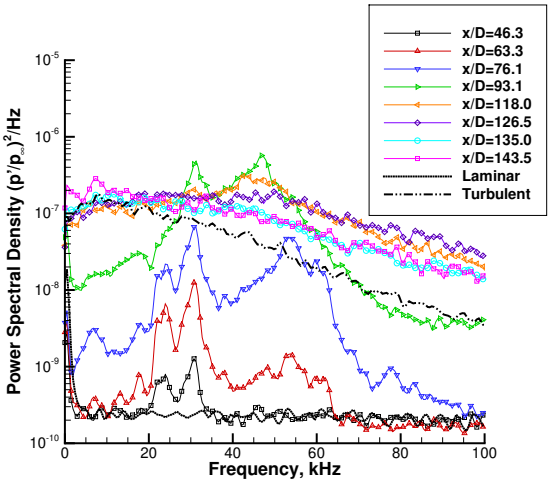

(c) $k = 3.05$ mm

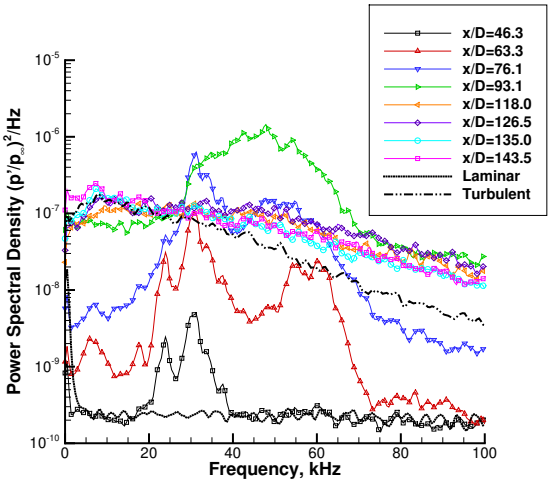

(d) $k = 3.18$ mm

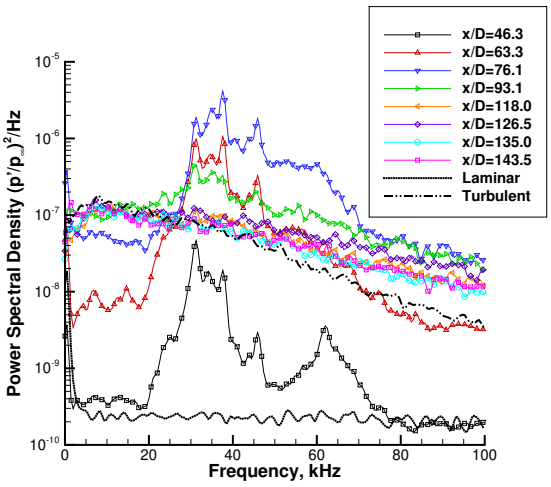

(e) $k = 3.30$ mm

Figure 3. Power spectra of surface pressure at various streamwise positions along the roughness wake centerline. Several runs with a stagnation pressure of 88 psia.

new calibrations were obtained in situ during each entry. The calibrations were not observed to vary significantly. Note that the sensors at $x/D = 93.1$, $x/D = 126.5$, and $x/D = 143.5$ were operational in July 2011 but were broken during the October 2011 entry.

The spectra near transition do not repeat well. Slight changes in tunnel noise may account for the uncontrolled repeatability of transition due to small, nearly-critical roughness. However, a reading of tunnel noise is not taken during the run as insertion of a pitot probe would perturb the flowfield. It is possible that changes in the nozzle temperature between runs could affect the repeatability. The nozzle temperature has been observed to increase from approximately 25 °C to 35 °C throughout the day after performing several runs. This increase in heating occurs after each run as the heated air from the driver tube blows down into the vacuum tank. Thus, the first run of the day will have the lowest nozzle temperature and (in general) the final run of the day will have the highest nozzle temperature. A higher nozzle temperature could cause the boundary layer to thicken and change the effect of the roughness on transition. Table 1 lists the run number for a particular day as well as the average temperature reading of 29 thermocouples on the outer surface of the nozzle. The thermocouples were located at 90° azimuthal increments at axial locations of 0.17–1.71 m from the throat. An accurate temperature distribution on the interior of the nozzle cannot be obtained during the run because any instrumentation could damage the nozzle surface or trip the nozzle boundary layer. Preliminary analysis of the boundary-layer thickness and roughness Reynolds number using the Harris code[12] shows that the effect of nozzle-wall temperature is probably not significant enough to account for the uncontrolled repeatability. However, further analysis is needed.

In Figure 4(a) for $k = 2.79$ mm, repeatability of the surface-pressure fluctuations is shown to be poor. At $x/D = 118.0$ and $x/D = 135.0$ in particular, the amplitudes from runs B and C were higher than for run A, indicating that transition was occurring farther upstream for runs B and C. All three runs show a peak near 23 kHz; it is just the amplitudes that appear different. It is unknown why the repeatability is poor for this case. Transition occurs farther forward for run C, which had the warmest nozzle temperature. However, a warm nozzle would theoretically cause a thicker boundary layer, lowering the height ratio $k/\delta_{0.995}$ and the roughness Reynolds number such that transition would be delayed. There may be additional effects from the changing roughness profile on the instabilities. Nevertheless, it appears that the nozzle temperature is not a likely cause of the poor repeatability, at least for the $k = 2.79$ mm results here.

For the 3.05-mm roughness, the repeatability is markedly better (Figure 4(b)). The peaks and amplitudes in the spectra are more consistent between the three runs at this roughness height. In Figure 4(c) for $k = 3.30$ mm, the agreement appears even better than for $k = 3.05$ mm. Though preliminary results would seem to indicate that repeatability improves for roughness heights greater than 2.79 mm, additional runs are necessary to further explore the repeatability. It is possible that a roughness height of 2.79 mm for these conditions is within some range of heights where the effects of tunnel noise, wall temperature, stagnation pressure, or some other factor are highly critical.

E. Summary of Roughness Experiments

Surface pressure sensors are continuing to be used in the wake of a cylindrical roughness on the nozzle wall in an effort to characterize the instabilities leading to transition due to isolated roughness. A new set of instabilities have been detected that occur due to nearly-critical roughness elements, or roughness of small heights that cause incipient transition within the available measurement range. For a stagnation pressure of 88 psia, roughness heights of 2.79–3.30 mm appear to be the smallest heights that cause incipient transition on the nozzle wall within the spatial measurement range of the apparatus. Because these roughness heights are likely near the critical height, they represent an interesting test case for understanding transition due to critical roughness. Future plans involve introducing controlled disturbances into the wake of the roughness to determine the stability characteristics of the wake. The stability characteristics can then be compared to future computations in an effort to better understand transition due to critical roughness. Determining the effect of experimental parameters such as nozzle temperature on the instability amplitudes and transition location is vital to selecting a repeatable test case that can be compared to computations. Present efforts are focused on determining the repeatability of the pressure fluctuations for these small roughness heights and developing hardware that can be used to introduce artificial disturbances into the flow.

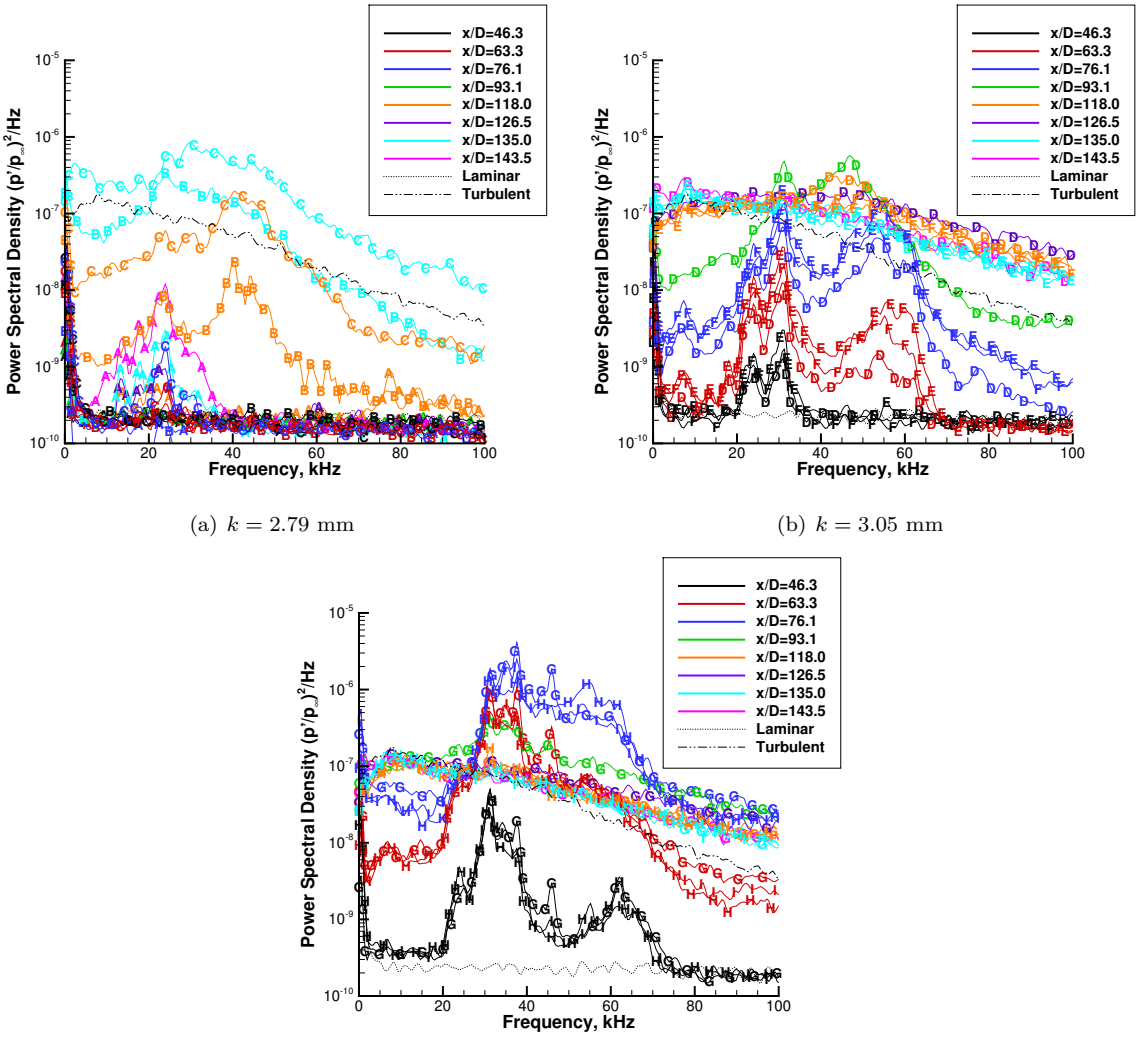

(a) $k = 2.79$ mm

(b) $k = 3.05$ mm

(c) $k = 3.30$ mm

Figure 4. Power spectra of surface pressure at various streamwise positions along the roughness wake centerline. Several runs with a stagnation pressure of 88 psia. Repeated runs are shown, with symbols denoting the run.

Table 1. Summary of tunnel conditions for repeated runs for roughness heights of 2.79, 3.05, and 3.30 mm. The "Run #" column indicates the daily run number, as the nozzle heats up after sequential runs. $T_{\text{avg,nozzle}}$ is the average of 29 thermocouples on the outer surface of the nozzle.

Run	k (mm)	Date	$p_{0,i}$ (psia)	Run #	$T_{\text{avg,nozzle}}$ (°C)
A	2.79	July 23, 2011	95.5	1	–
B	2.79	October 5, 2011	95.2	2	35.2
C	2.79	October 6, 2011	95.2	6	38.0
D	3.05	July 23, 2011	94.8	2	–
E	3.05	October 5, 2011	95.3	4	37.3
F	3.05	October 7, 2011	95.3	2	34.4
G	3.30	July 24, 2011	95.4	1	–
H	3.30	October 5, 2011	95.3	6	38.5
I	3.30	October 6, 2011	95.8	1	31.4

III. Testing an Improved Method for Determining Heat Transfer from Temperature-Sensitive Paint

A. Extracting Heat Transfer from Temperature-Sensitive Paint

Temperature-sensitive paints have been used to obtain global temperature distributions for many projects in the BAM6QT, but it is more useful to obtain quantitative heat transfer from the TSP. Prof. John Sullivan of Purdue University developed a method for calibrating the TSP to quantitative heat transfer using data from a single Schmidt-Boelter (SB) heat-transfer gauge.[15] A square patch of TSP is compared to data from a Schmidt-Boelter gauge, and the comparison patch should have a surface area similar to the SB gauge (0.123 m^2). Also the comparison patch should be at a location where the heat transfer is nominally the same. The local heat flux can be found using Fourier's law,

$$\dot{q} = -k\nabla T \tag{1}$$

where $\dot{q}$ is the local heat flux and k is the thermal conductivity of the insulating paint layer. The insulating layer is applied directly onto the model surface, beneath the TSP layer. To simplify Equation 1, it is assumed that the temperature varies only in the wall-normal direction, the temperature profile is linear, and the temperature at the base of the insulator (model temperature, T_{model}) is constant spatially and temporally. With these assumptions, Fourier's law can be simplified to a linear relationship

$$\dot{q} = \frac{k}{L}(\Delta T + T_i - T_{model}) \tag{2}$$

$$\Delta T = T - T_i \tag{3}$$

where L is the thickness of the insulating layer, T is the temperature of the surface during the run (obtained from the TSP), and T_i is the temperature of the model just before the start of the run. T_i can be obtained from the two thermocouples present in the SB gauge. The calibration method works by utilizing a least-squares method that finds the values of k/L and T_{model} that yield the best agreement between the calibrated TSP and the data from the SB gauge. According to the definitions of T_{model} and T_i, and the assumption of a temporally constant model temperature, these two temperatures should nominally be the same. However, T_{model} is chosen to best fit the data, regardless of how much it varied from T_i. See References 16, 17 and 18 for more information on temperature-sensitive paints and obtaining quantitative heat transfer in the BAM6QT.

In several plots, the non-dimensional heat transfer (Stanton Number) will be shown. The Stanton number is defined as

$$St = \frac{\dot{q}}{\rho_\infty u_\infty \left(H_0 - h_w\right)} \tag{4}$$

$$H_0 - h_w = \left(c_p T_\infty + \frac{u_\infty^2}{2}\right) - c_p T_w \tag{5}$$

where ρ is the density, u is the velocity, h is the enthalpy, H is the total enthalpy, T is the temperature and c_p is the specific heat. The subscripts 0, w and ∞ denote the total, model wall and freestream values, respectively.

B. Paint Thickness Measurements

It is important to obtain an accurate measurement of the paint thickness to verify the constant-paint-thickness assumption. A method to measure the paint thickness on a curved surface was devised using an Elcometer 456 capacitance gauge. The raw numbers from the gauge are not necessarily accurate on a curved model surface since the capacitance gauge sensing surface is flat. As the curvature of the model surface increases, the error in the gauge measurements increase. To test the accuracy of the gauge, a roll of 3M 471 vinyl tape was used, with a known thickness of 127 μm. The vinyl tape was first placed on a flat metallic surface. Measurements were taken at 10 random locations on the bare metallic surface, giving an average reading of 0.6 μm. Thickness measurements were then taken at 10 random locations on the vinyl tape, giving an average reading of 125 μm. The gauge appears to have a high accuracy when measurements are taken on a flat metallic surface.

The next test was done with the vinyl tape placed on a 7° half-angle cone. The tape was placed along the surface of the cone in the axial direction. Measurements of the tape thickness were taken at 4 inches to 15 inches from the nosetip, at 1-inch intervals. Measurements were then taken on the bare surface of the cone, at the same axial locations. The results are shown in Figure 5. The red symbols are the thickness of the tape measured by the capacitance gauge. The green symbols are the thickness measured by the gauge when placed on the bare aluminum surface. When the gauge is placed on the bare aluminum surface, the thickness readings should theoretically be zero, but error is introduced due to the curvature of the cone. Note that the error is greater further upstream, since the curvature of the cone increases towards the nosetip. The non-zero thickness measured by the gauge on the bare metallic surface will be referred to as the "thickness offset". The blue symbols are the offset thickness subtracted from the measured thickness. The solid black line is the actual thickness of the tape. The maximum error between the blue symbols and the actual thickness is about 6%. The error in the offset subtraction method tends to get larger near the nosetip due to the increase in the surface curvature.

C. Paint Feathering

In previous experiments,[6,17,19] TSP was added to the frustum of the cone, with the nosetip removed. Therefore, when the nosetip was installed, there would be a forward-facing step of about 200 μm created by the addition of the TSP at the nosetip-frustum junction. The slope at this forward facing step was roughly 900–1200 μm/mm, as measured with a Mitutoyo SJ-301 surface roughness tester.

A new method of painting, where the paint is feathered at the leading edge, is used in the current set of experiments. The nosetip is left installed in the model during the painting process. The paint is sparingly added to the nosetip region, and then sanded down so there is a smooth gradual increase of paint thickness going from the bare upstream tip of the nose to the frustum. The slope measured with the surface roughness tester is typically near 5–10 μm/mm. This new paint feathering technique appears to have essentially eliminated the forward-facing step created by the paint, but future tests need to be done to confirm if there is a residual effect created by this much-reduced forward-facing step.

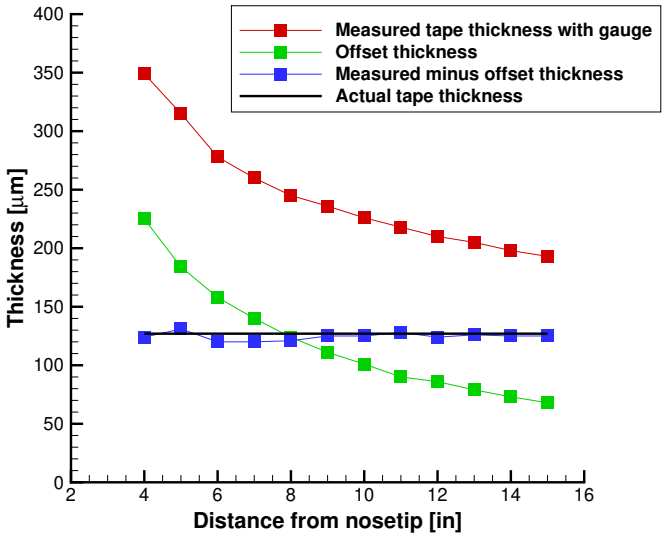

Figure 5. Measurements of tape thickness on the surface of a 7° half-angle cone.

D. Heat Transfer Results

Experiments were performed with a nominally sharp 7° half-angle cone at 0° angle of attack with temperature-sensitive paint and six Schmidt-Boelter heat transfer gauges. The experimental heat transfer can be compared to a theoretical solution developed by Prof. John Sullivan of Purdue University and Prof. Tianshu Liu of Western Michigan University. The theoretical solution is only good for laminar flow, and utilizes a compressible-boundary-layer similarity solution found in Reference 20. The viscosity was modelled using the work of Lemmon and Jacobson.[21] The outer flow conditions were provided by solving the Taylor-Maccoll equations for conical flow.[22] Previous experiments showed that the heat-transfer reduction method worked well if the SB gauge used to anchor the TSP was accurate.[23] Approximately half of the gauges used in these previous experiments yielded heat transfer that agreed well with theory. These sensors were sampled at 50 kHz by the oscilloscopes in Hi-Res mode.

New experiments were performed in August 2011, with the gauges sampled at a much lower rate of 50 Hz. The SB gauges do not have a very high frequency response, therefore sampling at 50 kHz was not necessary. The lower sampling rate also allows for more averaging, thereby reducing random noise in the output signal of the SB gauge. In hindsight, a sampling rate of 500 Hz would have been best, since this would allow for a reduction in random noise from sampling at 50 kHz, but would also allow for the peak in heat transfer during tunnel startup to be fully captured. Capturing this peak may prove to be useful for future data processing.

The first set of tests did not produce good results, with many of the gauges showing heat transfer more than 20% above the theoretical heat transfer (Case 1 in Figure 6). Figure 6 shows the non-dimensional heat transfer plotted against axial distance along the cone. It was noticed that several of the gauges in Case 1 were not flush with the cone, and the last gauge was protruding by roughly 300 μm. It was decided to remove the model from the tunnel, and reinstall the last gauge. The step created by the last gauge was reduced to about 30 μm when reinstalled. Case 2 in Figure 6 shows that the furthest downstream gauge is in better agreement with the theoretical heat transfer. This is an expected result, as a gauge protruding into the boundary layer would most likely measure a higher heat transfer than a gauge flush with the surface. Note that the first four gauges agree very well between Cases 1 and 2. Also note that the 5th gauge was broken during the second model installation, so no data was gathered from this gauge for Case 2.

After this second set of tests, it was then decided to reinstall all the Schmidt-Boelter gauges. Table 2

lists the steps created by each gauge for each case. The steps were measured using a Mitutoyo SJ-301 surface roughness tester. All the gauges were installed as flush as possible for Case 3. Table 2 also lists the calibration range for each sensor. Case 3 in Figure 6 shows the heat transfer obtained from this third test. Five of the six gauges are within 20% of the theoretical heat transfer. It is not clear whether the reduction of measurement noise by lowering the sampling rate or the more flush mounting of the gauges had a more significant impact. It seems likely that having a flush gauge is more important, but regardless both measures should be taken in future tests. Only gauge SB–E shows heat transfer more than 20% above the theoretical. This gauge was sent back to the Medtherm Corporation in October 2011 to check the factory calibration. The theoretical heat transfer at the axial position of the first gauge and the last gauge is approximately 2.0 and 1.75 kW/m^2. This heat transfer is much lower than seen in other hypersonic wind tunnels. The low heat transfer in the BAM6QT sometimes causes problems in the heat transfer calibration method.[24]

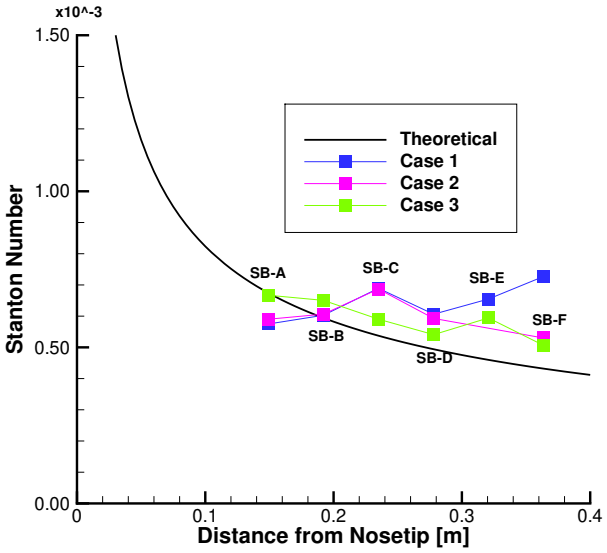

Figure 6. Heat transfer from SB gauges with varying protuberance heights into the boundary layer. p_0 = 131 psia, $\mathrm{Re}_\infty = 9.9 \times 10^6$/m. Quiet flow.

Table 2. Step created by the heat transfer gauges.

Position	Distance from Nosetip	Gauge Letter	Calibration Range	Case 1 Step	Case 2 Step	Case 3 Step
1	0.149 m	SB–A	0–22 kW/m^2	-10 μm	-10 μm	+8 μm
2	0.192 m	SB–B	0–22 kW/m^2	-26 μm	-26 μm	-10 μm
3	0.235 m	SB–C	0–11 kW/m^2	+40 μm	+40 μm	+5 μm
4	0.279 m	SB–D	0–22 kW/m^2	-26 μm	-26 μm	-19 μm
5	0.321 m	SB–E	0–22 kW/m^2	-10 μm	-10 μm	+10 μm
6	0.363 m	SB–F	0–11 kW/m^2	+300 μm	-30 μm	+5 μm

A TSP image from Case 3 is shown in Figure 7. The boundary layer is most likely laminar since the TSP shows a low, even level of heating. The higher heating near the nosetip is due to the thinner boundary layer. Figure 8 shows the calibrated heat transfer from the TSP using SB–D for Case 3, along with the heat transfer obtained from the six heat transfer gauges and the theoretical heat transfer. The linear heat

transfer calibration method appears to work well over most of the axial length of the cone. Data was not included near the nosetip because the TSP was sanded down in this region. Figure 9 shows the heat transfer from SB–D over the course of a run, along with the calibrated TSP at the comparative patch. The curve fit algorithm works well in matching the data from the TSP with the heat transfer from the SB gauge.

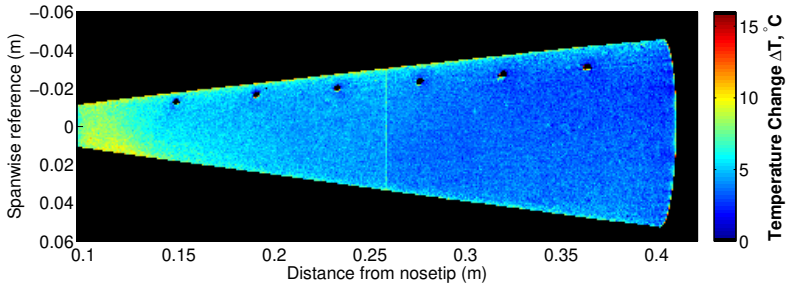

Figure 7. TSP image of the 7° half-angle cone at 0° angle of attack. Case 3 from Figure 6. p_0 **= 131 psia,** $\mathbf{Re}_\infty = 9.9 \times 10^6$**/m, quiet flow.**

.

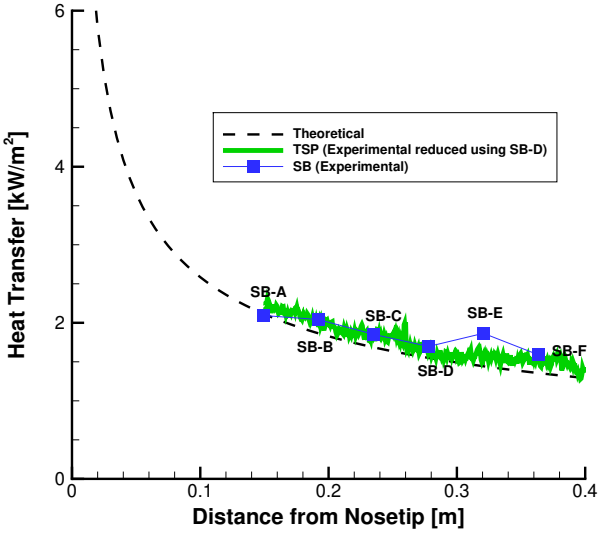

Figure 8. Heat transfer rates calculated from TSP with the reduction method and compared to theory. p_0 **= 131 psia,** $\mathbf{Re}_\infty = 9.9 \times 10^6$**/m, quiet flow.**

1. Reducing Heat Transfer from TSP Using Known Paint Thickness and Model Temperature

The final set of tests examined the possibility of calibrating the TSP to heat transfer using the measured paint thickness and the measured model temperature. For this case, T_{model} and T_i are assumed to be equal; therefore the heat transfer equation reduces to

$$\dot{q} = \frac{k}{L}\Delta T. \tag{6}$$

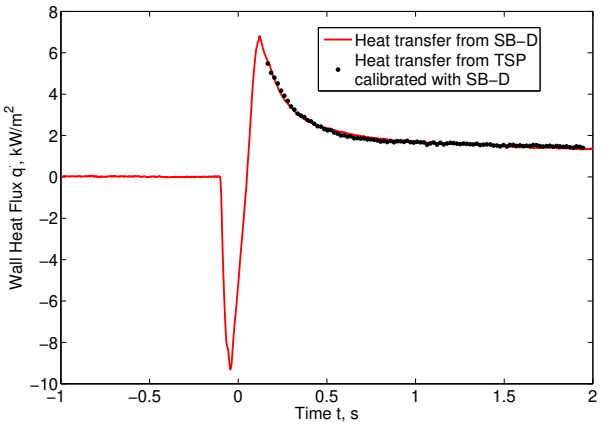

Figure 9. Plot of heat transfer from SB–D along with the heat transfer calculated at the comparison patch of TSP. Case 3 from Figure 6. $p_0 = 130$ psia, $\mathrm{Re}_\infty = 9.9 \times 10^6$/m, quiet flow.

According to Prof. Tianshu Liu, the thermal conductivity (k) for the insulating paint is between 0.21 and 0.50 W/m-K, with a typical value being 0.25 W/m-K.[25] The paint thickness was measured using an Elcometer 456 capacitance gauge and the method discussed in Section B. The paint had an average thickness of 201 μm with a $\pm 5\%$ variation from the mean.

Figure 10 shows the results with the heat transfer calibrated from the TSP with the linear reduction method (green curve). This plot also shows the heat transfer calculated with the known paint thickness, thermal conductivity, and model temperature (red and turquoise curve). The thermal conductivity was chosen to be 0.25 W/m-K. The turquoise curve is the lower limit of the calculated heat transfer assuming the paint thickness is 5% below the mean, and the red curve is assuming the paint thickness is 5% above the mean. From this plot, it can be seen that the calibration method needs to be anchored with a SB gauge due to the large error in the red and turquoise curves. Even if the 0.21 W/m-K is used as the thermal conductivity, the error is still large. It is not clear if the error is largest in the estimated thermal conductivity, the measured model temperature or the measured paint thickness.

IV. Forward-Facing Cavity Resonance in Quiet Flow

A. Introduction

The forward-facing cavity was originally used as a passive method of reducing the stagnation point heat flux for high-speed missiles.[26] Dynamic pressure measurements within the cavity showed that the forward-facing cavity resonated and that the bow shock oscillated at the same resonant frequencies. Cavity oscillations are always large under conventional noise. Ladoon et al.[27] showed experimentally that these oscillations exist in low-noise environments as well. However, the oscillations are small under quiet flow for shallow cavities.

At some critical depth, self-sustained resonance of the cavity occurs, where noise is damped very little or not at all. Ladoon[27] attempted to find this critical length in the Purdue Quiet Flow Ludwieg Tube (Mach-4 Tunnel) using a controlled laser perturbation. Ladoon ran experiments with and without a controlled perturbation but found that his maximum possible cavity depth was too short to study the critical depth characteristics. Using extrapolation, Ladoon calculated the critical depth of the cavity to be about $L/D = 2.7$. Segura[28] used a model with a longer maximum possible cavity length of $L/D = 3.0$ in the same tunnel and found self-sustained resonance at cavity depths greater than $L/D = 1.3$. Ladoon and Segura found that the cavity was very sensitive to the presence of freestream disturbances and that the amplification of these disturbances increases with the cavity depth. Numerical simulations by Engblom, et al.[29,30] showed that shorter cavity depths require some freestream noise to cause resonance. For longer cavity depths, resonance

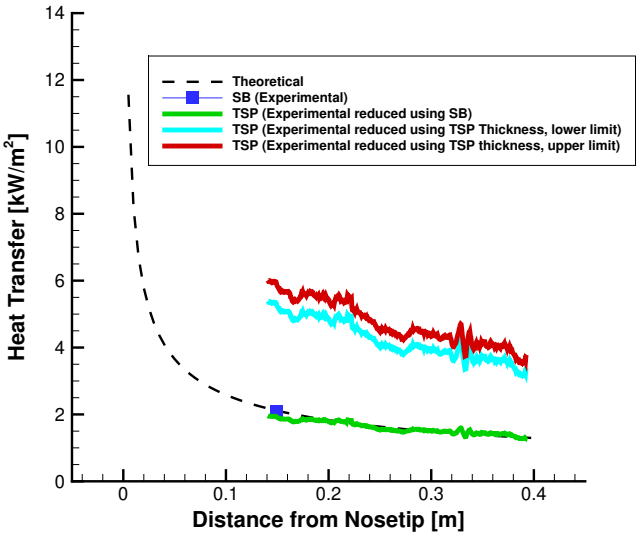

Figure 10. Heat transfer rates calculated from TSP with the reduction method and known paint thickness and model temperature. p_0 = 131 psia, $\mathrm{Re}_\infty = 9.9 \times 10^6$/m, quiet flow.

was obtained with little or no freestream noise.

Experiments and computations have found that the primary resonant frequency for the forward-facing cavity is that of a standing wave in a resonance tube.[29–33] This resonant frequency is given by the expression:

$$f_{1n} = \frac{\omega_{1n}}{2\pi} = \frac{a_0}{4L^*} \tag{7}$$

where a_0 is the speed of sound within the cavity and $L^* = L + \delta$ is the adjusted cavity depth. L is the depth of the cavity and δ is the average bow-shock stand-off distance. The flow velocity in the cavity is assumed to be small so that the stagnation temperature can be used to estimate the speed of sound. A bow-shock stand-off distance of $\delta/D = 0.24$ can be used for the forward-facing cavity.[28] This is an approximation, using a value between that of the shock stand-off distance of a three-dimensional cylinder with a flat nose and that of a hemisphere.[34]

B. Model and Instrumentation

A forward-facing cavity model designed by Rodrigo Segura[35] was used in the BAM6QT (Figure 11). The model is a hemisphere with 19.05 mm radius and a 19.05-mm-diameter circular cavity. The depth of this cavity is adjusted via a cylindrical steel insert, which can be slid forward or aft in the cavity and secured with set screws. The maximum depth of the cavity is about $L/D = 5.00$, or 95.25 mm. One B-screen Kulite XCQ-062-15A pressure transducer was mounted in the center of this steel insert. Since the Kulite was mounted in a "pitot configuration," or facing directly into the flow, a B-screen Kulite was used to protect the sensor from particle impact. Each cavity depth was run in quiet flow, then again in noisy flow, at an initial stagnation pressure of 1114.2 ± 3.4 kPa and an initial stagnation temperature of 159.6 ± 5°C. The uncertainties in these conditions are simply the variation between each of the runs.

C. Data Analysis

Different cavity depths from $L/D = 0$–5.00 were tested. Time traces for a shallow cavity (black trace) and a deep cavity (red trace) are given in Figure 12. The blue trace in Figure 12 is the black trace magnified

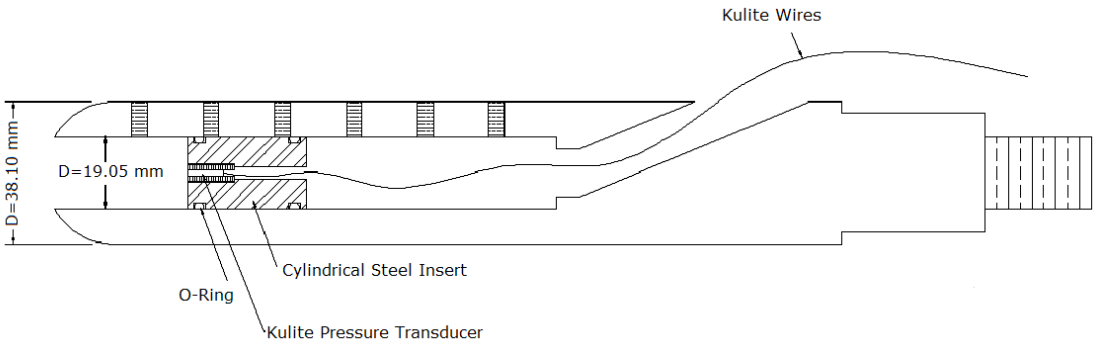

Figure 11. Schematic of forward-facing cavity model.

100 times to better show the pressure fluctuations measured at the same condition. Very little resonance is exhibited by the short cavity. While there may still be some resonance of the shallow cavity, a cavity will not be considered to be "self-resonating" in this paper unless the amplitude of that resonance is significant compared to pitot-pressure fluctuations under the same conditions. A significant amplitude of resonance is determined by comparing the normalized RMS amplitudes of several different cavity depths with measurements of freestream noise with a pitot tube.

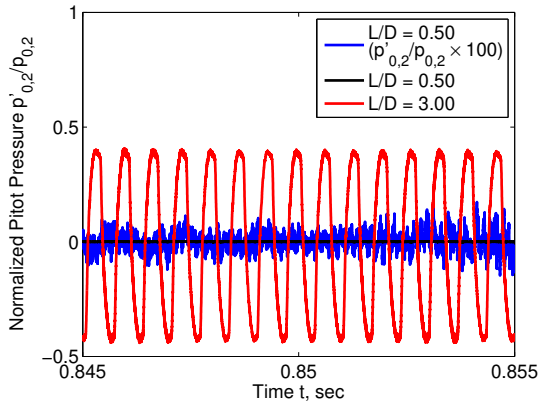

Figure 12. Time trace of shallow cavity (black trace) and deep cavity (red trace) in quiet flow.

Since the Kulite pressure transducers are mechanically stopped at pressures above 15 psia, they do not provide readings at full stagnation pressure. Therefore, traces were taken at vacuum pressure with no flow to find the spectra of the baseline electronic noise. The root-mean-squared spectra of the two different cavity depths at the same condition and a vacuum trace are given in Figure 13. Power spectra are computed for 0.1-second samples using Welch spectral estimation and Blackman windows. Fast Fourier transforms (FFTs) of 0.2-second segments with up to 50% overlap were taken and averaged together to form the power spectrum. A table of calculated RMS values and the frequency band used for integration is provided in Table 3. The resonant frequency is measured as a peak near the expected organ-pipe frequency. The black trace in Figure 13 corresponds with a cavity depth of $L/D = 0.50$, where there should be no self-sustained resonance. There is, however, a peak at around 6 kHz, which is the cavity depth's expected resonant frequency. This is considered a weak resonance of the cavity, but not a clear self-sustained resonance. The red trace corresponds with a cavity depth of $L/D = 3.00$, where there is a clear self-sustained resonance. This is shown by the large fundamental peak at about 1.5 kHz and the presence of large harmonics of the

fundamental frequency. The presence of these large, sharp peaks indicates large amplitudes of sinusoidal frequency content. The RMS amplitude of the fundamental peak is about 31% of the mean pitot pressure ($p'_{0,2}/p_{0,2} = 0.31$), which is about four orders of magnitude larger than the pitot-probe trace.

Table 3. RMS amplitudes for selected cavity depths in quiet flow

L/D	Frequency Band for Integration (kHz)	RMS/mean ($p'_{0,2}/p_{0,2}$)
Pitot Probe	6.16–6.87	1.57×10^{-5}
0.50	6.16–6.87	1.82×10^{-4}
3.00	1.46–1.56	0.308

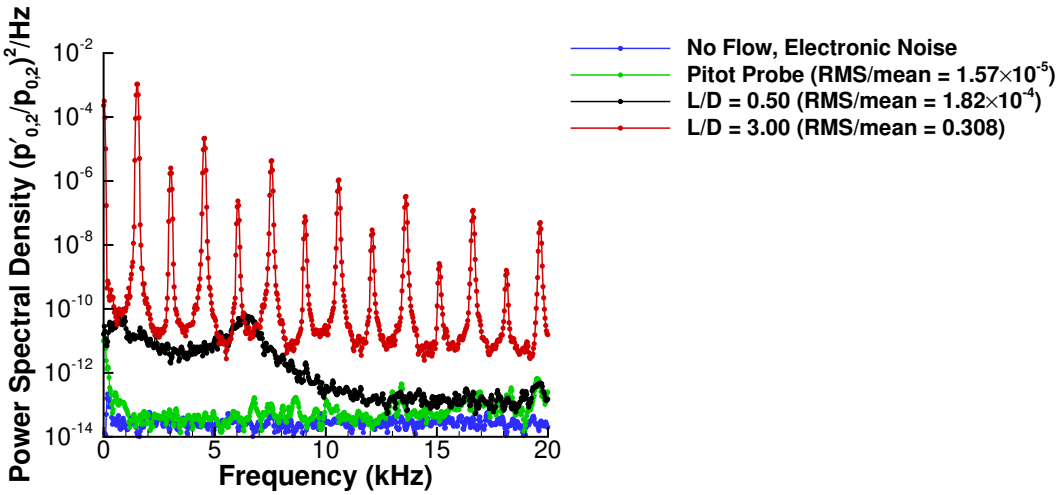

Figure 13. Effect of cavity depth on resonant frequency measured.

Figure 14 shows the measured fundamental frequency for various cavity depths and compares them to the expected theoretical values. At shallow depths, where $L/D < 1.00$, the measured fundamental frequency differs from theory by 9–21%. For deeper cavities, where $L/D \geq 1.00$, the measured fundamental frequency differs by 9–11% from theory. Noisy flow measurements of the fundamental frequency differ from quiet flow measurements by 5.6% at most. This indicates that the measured resonant frequency agrees fairly well with theory for deep cavities. The small discrepancy between the measured and theoretical fundamental frequency could come from the estimation of the bow-shock stand-off distance.

The measured pressure fluctuations are normalized by the measured mean pitot pressure. The root-mean-square of the pressure fluctuations is calculated by taking a power spectra of the normalized pressure fluctuations, integrating the power spectra of the fundamental peak across the full width at half the maximum value, and then taking the square root of this integral. These data are given in Figure 15. Figure 15(a) shows shallower cavities ($L/D < 1.5$) with the vertical axis expressed on a logarithmic scale. Typical pitot-probe measurements of freestream noise on the centerline at similar conditions are shown by a gray dashed line for quiet flow and a gray dash-dot line for noisy flow. The RMS pressure fluctuations for the pitot-probe measurements are taken by integrating across 6.16–6.87 kHz. This is the same range of frequencies used to find the RMS pressure fluctuations for $L/D = 0.50$. The noise level for the pitot-probe measurements is one order of magnitude less than similar measurements made by Steen.[36] This is because Steen integrated from 0–60 kHz to find the RMS pressure fluctuations. Noisy flow data are in red circles and quiet flow data are in blue squares. RMS fluctuations for deeper cavities, where $L/D > 1.0$, are presented on linear axes in Figure 15(b). The pitot-probe measurement of freestream noise is not presented in this graph because it

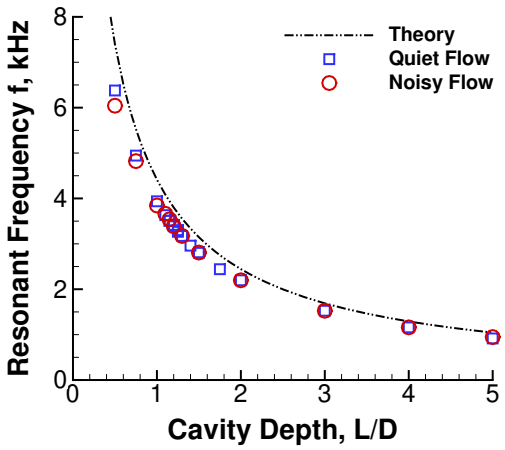

Figure 14. Effect of cavity depth on resonant frequency measured.

would be indistinguishable from the horizontal axis at this scale. The noisy flow data are again shown by the red circles and quiet flow data are shown by the blue squares.

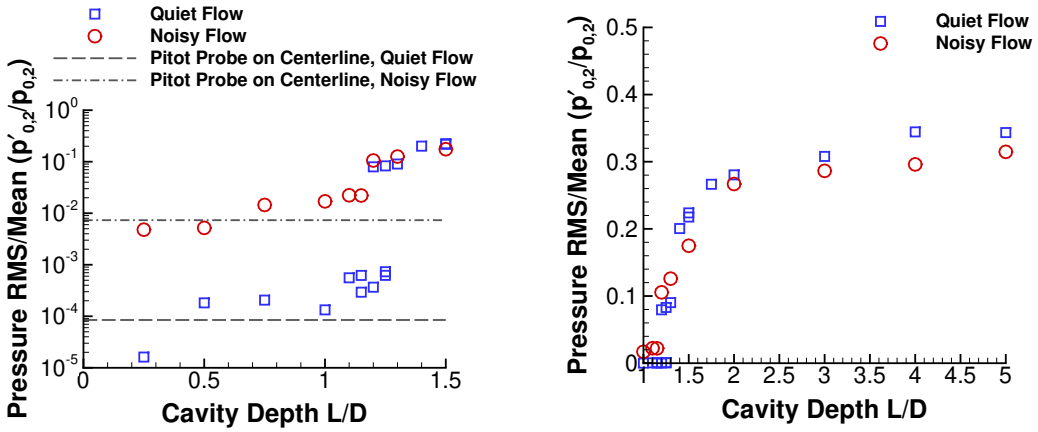

(a) Shallower cavities: $0 < \frac{L}{D} < 1.5$ (semi-log scale)

(b) Deeper cavities: $1.0 < \frac{L}{D} \leq 5.0$

Figure 15. Change in normalized RMS pressure fluctuation with change in cavity depth.

The RMS pressure fluctuations appear to be similar to the pitot-probe measurements of freestream noise for cavity depths up to $L/D = 1.15$. At $L/D \geq 1.15$, the fluctuations measured in the forward-facing cavity in quiet flow are about the same in magnitude as those of the noisy-flow fluctuations. At these depths, the quiet flow RMS pressure fluctuations increase by at least two orders of magnitude. At shallower cavity depths ($L/D \leq 1.15$) the noisy-flow RMS pressure fluctuations are higher than in quiet flow, which is expected. However, it is interesting to note that for deeper cavity depths, where self-sustained resonance occurs, the noisy-flow fluctuations are slightly lower in magnitude than those under quiet flow. The reason for this is unknown. It is possible that three-dimensional fluctuations break up the resonance and therefore cause lower-magnitude pressure fluctuations in the cavity.

1. *Effect of Turbulent Spots*

A Sentex hot-film array mounted on the BAM6QT nozzle wall shows a turbulent spot (blue trace in Figure 16). The forward-facing cavity, which was not previously experiencing self-sustained resonance, shows the effect of this turbulent spot on the model. The red trace in Figure 16 represents the damped resonance created by the Mach wave radiated from the turbulent spot on the nozzle wall. This uncontrolled experiment is similar to the controlled laser-perturbation experiments previously done by Ladoon et al.[27]

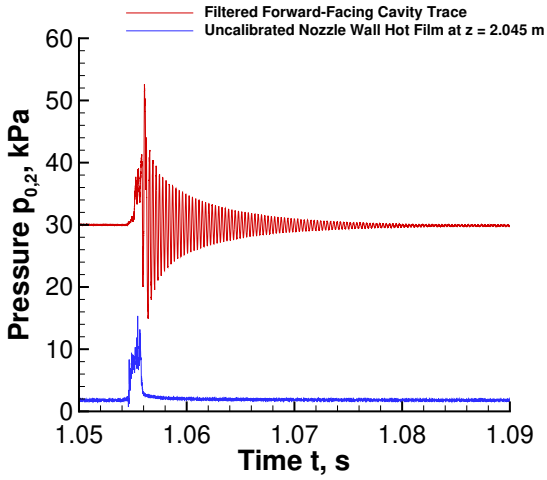

Figure 16. Effect of a turbulent spot on cavity resonance. $L/D = 1.15$, $p_0 = 1018.4$ **kPa,** $T_0 = 420.5$ **K.**

V. Development of 3-Inch Shock Tube for Sensor Calibration

A half-scale version of the 6-inch (15.2-cm) shock tube in the Graduate Aerospace Laboratories at Caltech (GALCIT)[37] has recently been designed and is nearing completion at Purdue. Much of the design work was completed by Kerlo.[38] This stainless-steel shock tube has a 8.9-cm inner diameter, a 3.6-m driven section, and a 0.9-m driver section. Figure 17 shows a rendering of the shock tube. The driven section is designed to reach pressures of 1 millitorr (100 Pa) or less, and the driver section can withstand pressures as high as 6895 kPa. The joints of the shock tube are designed to be smooth, so as to avoid disturbing the flow, in order to form a clean, planar shock wave followed by a clean laminar boundary layer.

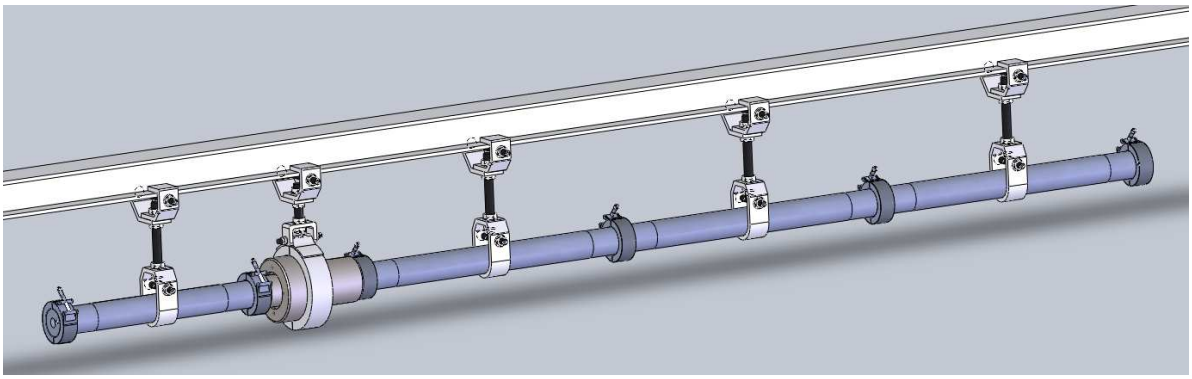

Figure 17. Rendering of the 3-inch new shock tube at Purdue.

The purpose of this shock tube is to calibrate sensors, especially PCB-132 sensors, for use in the BAM6QT and other hypersonic wind tunnels. Hypersonic boundary-layer instabilities often appear as high-frequency, small-amplitude fluctuations in pressure, heat transfer, and other quantities. Measuring these fluctuations accurately requires high-accuracy calibrations at high frequencies. If such calibrations are not provided by the manufacturer, a shock tube appears to be a good way to obtain them. This is because a shock wave approximates a step input in pressure, density, heat transfer, and velocity. In theory, a step input excites all the response frequencies of a system, allowing the determination of the entire frequency response using a single input. The calibration curve can be found by varying the strength of the shock wave.

PCB-132 sensors are piezoelectric pressure transducers designed to measure the time of arrival of shock waves. They have been of interest for hypersonic instability measurements since Fujii[39] showed that they were capable of measuring the second-mode instability. Since then, they have been shown to work in many hypersonic tunnels, performing the first measurements of second-mode waves in multiple tunnels, including some where such measurements were previously not feasible.[11,40–44] They are high-pass filtered at 11 kHz, with a quoted resonant frequency above 1 MHz. The manufacturer calibrates the sensors in a shock tube, by running one shock with a static pressure rise close to 7 kPa past the sensor. The calibration is assumed to be linear, with a 0 V offset.

This calibration technique is not necessarily sufficient for instability measurements. The frequency response of the sensors is left unknown, and it is not certain if the response at 7 kPa applies at the low amplitudes relevant to second-mode waves. The 3-inch shock tube was designed in order to answer these questions and enable accurate quantitative measurements of second-mode amplitudes.

The high frequencies and low amplitudes of second-mode waves mean that very thin and very low-amplitude shock waves are required to perform relevant calibrations. Lowering the initial pressure difference (driver pressure minus driven pressure) tends to weaken the shock wave (reduce the pressure rise across the shock), and increasing the initial pressure ratio (driver pressure divided by driven pressure) tends to decrease the thickness of the shock wave by increasing the Mach number. This means that thin, weak shock waves can be created by using very weak diaphragms that burst at low pressure differences, and reducing the driven pressure to a medium vacuum. Using the ideal shock tube equations to find the strength of the shock wave, and Taylor's solution for weak shocks to find its thickness, it is estimated that the weakest useful shock wave that can be created in this tube has a static pressure rise of 7 Pa, which is within the range of some large second-mode wave amplitudes in wind tunnels (estimated as 5-10 Pa from PCB measurements using the factory calibration). This weak shock wave will not be thin enough to excite high frequencies. Thinner shock waves can be created at higher driven and driver pressures, and this will be necessary to excite the higher frequency ranges of some sensors.

The 3-inch shock tube is currently nearing completion. Once finished, the actual vacuum and weak shock performance will be measured. A system using resistive heating to burst the diaphragms at lower pressure differences may be added at a later time.

VI. Measurements of Instabilities and Transition on a Flared Cone

The flared cone geometry has presented a unique platform for studying a nonlinear transition process in a hypersonic boundary layer. The flare of the cone maintains a nearly constant boundary layer thickness after the region of initial boundary layer growth, causing continuous amplification of second-mode waves in a narrow frequency band. These waves have been shown to reach N-factors up to 17 near the rear edge of the cone.[45]

The transition process creates a set of streamwise streaks of increased heating followed by a decrease in heating to near-laminar levels. At high enough Reynolds number there is a second increase in heating, and pressure fluctuation measurements indicate that the flow begins transitioning to turbulence. It has been hypothesized that this complicated process is due to interactions between the second-mode waves and streamwise vorticity, possibly as a result of the Görtler instability.[46] Fasel, et al. used DNS to show streak heating behavior due to nonlinear second-mode wave growth that resembles what has been seen in experiments.[47–49] Sivasubramanian and Fasel state, "The first peak in the skin friction roughly corresponds

to the streamwise location where the primary wave saturates. As the primary wave starts to decay following the nonlinear saturation, the skin friction decreases strongly. Then finally, a steep rise in skin friction occurs when all higher modes experience strong nonlinear amplification..."[47] Here the primary wave is at the most amplified frequency, and the skin friction is considered to be proportional to heat transfer.

Streamwise vorticity has also been introduced via small roughness elements placed on the cone, and a similar transition process has been observed.[45] However, the size and spacing of these roughness elements were not well controlled, so several methods for improving control are currently being investigated.

With the original flared cone model, transition could be seen at the rear of the model only at stagnation pressures above 160 psia.[23] The high pre-run pressure in the test section necessitated the use of two small port-hole windows for TSP image acquisition, instead of the larger rectangular window, which is only rated to 152 psia. The porthole windows limit the field of view on the model, which makes it difficult to obtain an image of the full transition process. Therefore, a longer flared cone model was fabricated that could achieve sufficiently high Reynolds number for transition, at a stagnation pressure that is low enough to allow the use of the rectangular window. The new model has the same flare as the old model, but it is 3-in. longer, which allows more of the transition process to be seen using the rectangular window at lower stagnation pressures. The longer model also increases the maximum attainable quiet Reynolds number by approximately 15 per cent. The data presented herein were obtained using the new, larger cone at a stagnation pressure of approximately 140 psia.

Figure 18 shows the cone's characteristic transition process, as described above. Sensors were not yet installed on the cone, so no heat transfer data is available. A streamwise temperature profile is plotted in Figure 19. This profile was taken along a ray approximately 6.5° below the centerline and it runs through the center of a streak. The shape of this profile is typical, but the absolute values of the temperatures vary from run to run. In this case, the maximum temperature change in the streak (at approximately 16-in.) is roughly three times greater than the temperature change in the laminar region upstream of 13.5-in. and it is roughly equal to the temperature change in the transitional region downstream of 19-in.

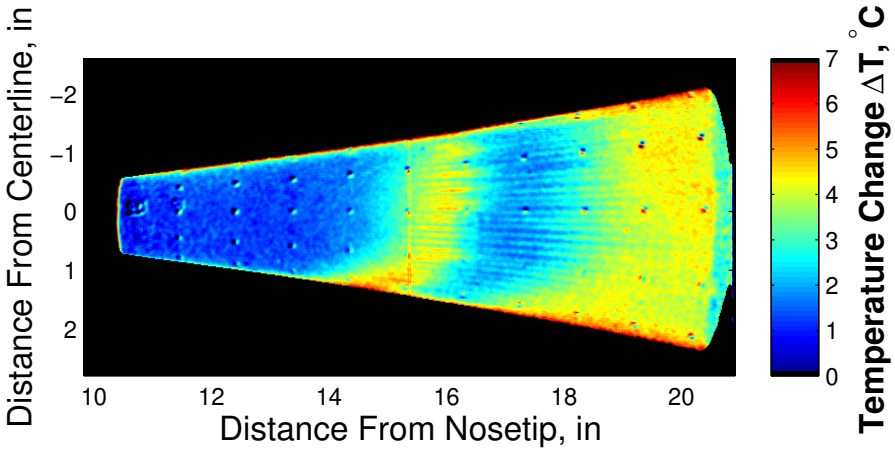

Figure 18. Typical TSP image at a stagnation pressure of 140 psia.

The temperature profiles at a fixed axial location are plotted in Figure 20 for two runs that were done back to back with the same cone orientation, and these two baseline cases repeat fairly well. The orientation of the cone can be identified by the fiducial mark that can be seen just above the centerline registration mark (the small black dot) at $x = 11.5$ in. in Figure 18. The fiducial mark is the number "01," which appears blurry in TSP images, but can be clearly seen in the raw pictures.

The cone was rolled up and down by 30° relative to the baseline orientation to determine whether the

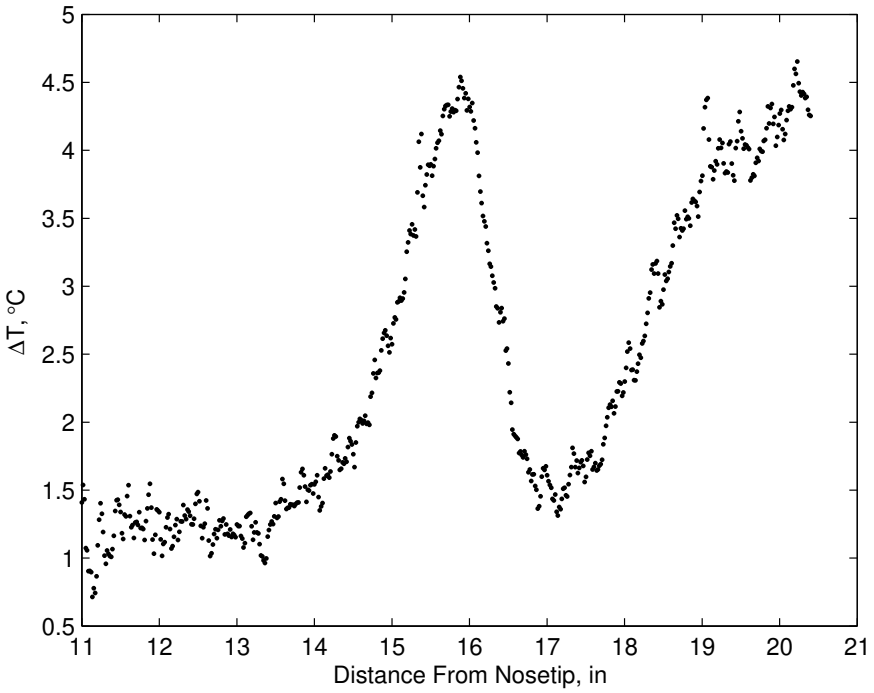

Figure 19. Temperature change along a ray.

streaks are body-fixed. Figure 21 shows a typical temperature profile from each orientation, plotted in body-fixed coordinates relative to the fiducial mark. The temperature profiles were also normalized by their respective maximum temperatures for ease of viewing. It's clear that the streaks line up, indicating that they originate with small roughness features on the cone's surface, rather than freestream disturbances.

The average angle between temperature peaks for the data plotted is shown in Table 4. Averages over each run were calculated over 14 streaks for the baseline cases (fiducial mark on window centerline), and 7 streaks for the rolled cases (fiducial mark $\pm$ 30° from the centerline). Streak widths and standard deviations (STD) of streak widths are rounded to the nearest tenth of a degree, and wavenumbers are rounded to the nearest integer.

The streak widths are consistent from run to run for each configuration, and the variation in streak widths across the three configurations is roughly 10 per cent. Again, this indicates that the streaks are induced by natural surface roughness, and therefore can be controlled through the application of roughness elements.

Table 4. Average Streak Separation and Wavenumbers

Orientation	Streak Width	STD of Streak Width	Wavenumber
Centerline	4.8°	1.1°	76
Centerline	4.8°	1.1°	76
30° down	5.0°	1.1°	72
30° down	5.0°	1.3°	72
30° down	4.9°	1.4°	74
30° up	4.5°	0.9°	80
Average	4.8°	1.1°	75

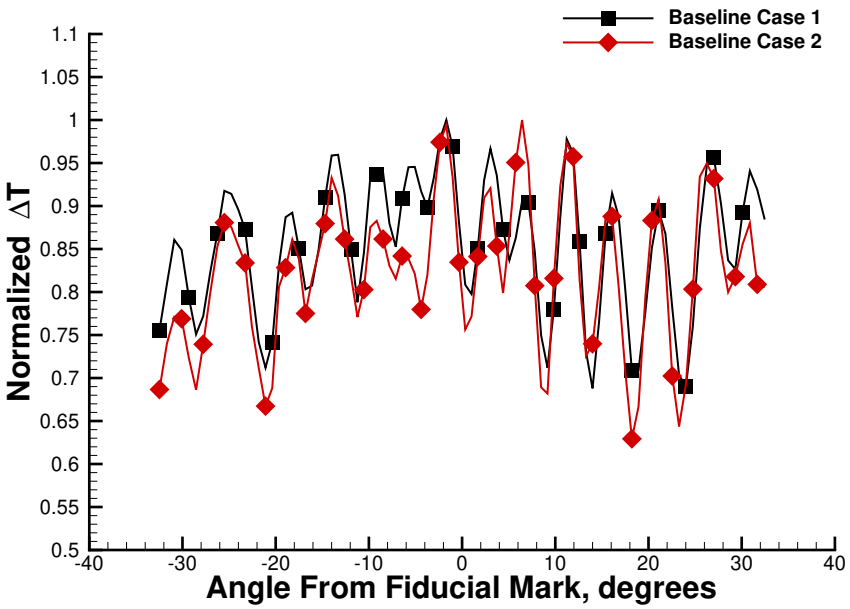

Figure 20. Spanwise Temperature Profiles

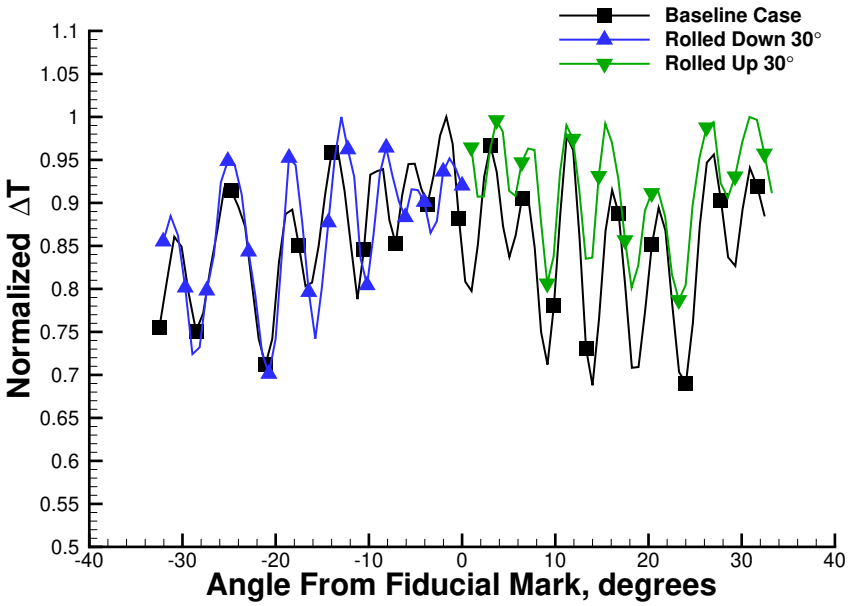

Figure 21. Spanwise Temperature Profile on Cone at Different Roll Angles

A. Improved Roughness Application Techniques

At the moment, there are computations that show heating patterns on the flared cone that resemble what is seen in experiments. However, the input disturbances in the experimental setup cannot yet be controlled to the same precision as in a computation, so the results from each method cannot be directly compared. It is therefore necessary to develop a method for applying uniformly sized and spaced roughness elements so that a precise input disturbance can be closely approximated. Three such methods are under development.

Firstly, a thin crenellated aluminum wafer that fits between the nosetip and frustum has been fabricated such that the teeth protrude from the surface of the cone and act as roughness elements. While the concept is simple, the wafer is small enough that machining it becomes difficult and the finished product is fairly delicate, resulting in imperfections in the teeth. This method is still being tested, and it is yet unknown whether these imperfections are significant to streak formation and control. Furthermore, the particular wafer that is being tested took roughly 2 days to machine, too long for this method to be a viable long-term option.

Secondly, dry rub-on transfer dots were custom-printed, as in Hunt and Saric.[50] While the diameter of the dots is controllable, their height is not, and it varies between printings. These have not yet been tested.

Thirdly, an electronic fluid dispensing system was obtained to dole out small volumes of a specialized epoxy to create uniformly sized roughness elements. A rotary stage was also acquired to allow the cone to be precisely rotated to less than a tenth of a degree in order to control dot spacing. The apparatus has not yet been tested.

VII. Effect of Nosetip Roughness on Transition for a Blunt 3° Cone

A. Effect of Nosetip Roughness on Transition for a Blunt 3° Cone

The effect of nosetip bluntness on transition has been studied in multiple experiments, including that of Müller and Henckels.[51] Nose radii of 1 mm to 15 mm were tested on a 1-m-long 2.89° half-angle cone. Experiments were performed in the H2K hypersonic blowdown tunnel in Cologne, Germany at Mach 6 and Reynolds numbers from 4×10^6/m to 20×10^6/m. Initially, transition location moved aft on the cone with an increase in nose radius. However, when a certain bluntness was reached, the trend reversed and increased nose radius led to a forward movement of the transition location.

A similar cone with a 3° half-angle and a 9.9-cm base diameter was used in the BAM6QT in an attempt to make a comparison to Müller's results. Preliminary experiments were performed by Gilbert and Steen,[52] but issues were encountered with the temperature sensitive paint, and transition location could not be visualized using this method. A spectral analysis was performed in an attempt to determine if instability waves were present, but no computations were available for comparison. A tunnel starting analysis was performed, and it was found that a gap in the pipe insert was necessary to start the tunnel when using a 15 mm nosetip on the model.

The present experiment continues the work in the BAM6QT to determine if transition can be observed on the blunt 3° cone. All testing occurred at 0° angle of attack, and tunnel runs were performed under conventional tunnel noise conditions. A variety of roughness heights and configurations were used on a 15-mm radius nosetip to induce transition. Distributed roughness with average RMS roughness heights of 20 μm and 140 μm and isolated roughness element heights of 130 μm and 380 μm were added to the smooth nosetip. Data were acquired using TSP and SB gauges. The SB gauge data were used to convert the TSP temperature data to heat transfer rate, as in Section III.

The TSP showed a region of high heat transfer beginning near 0.61 m from the nosetip of the model (Figure 22(a)). The curved vertical lines near 0.38 m, 0.46 m, and 0.66 m from the nosetip are due to light reflections off the windows and are not part of the flow. The onset of higher heating did not vary significantly in position with a change in Reynolds number, as seen in Figure 22(b).

Streamwise heat transfer profiles were created by averaging 10 pixels in the spanwise direction with a moving average of 5 pixels in the streamwise direction. Streamwise profiles for the two images of Figure 22 are compared in Figure 23. For both Reynolds numbers, the onset of higher heat transfer rate occurs near

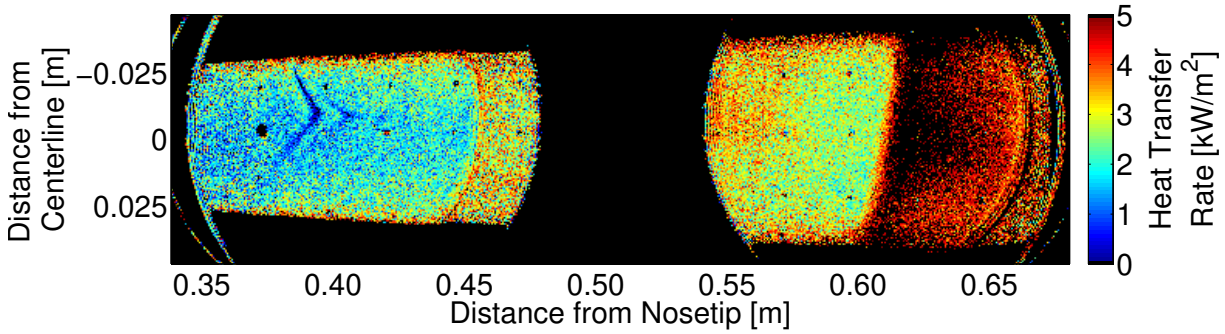

(a) $Re = 1.6 \times 10^7/\mathrm{m}$

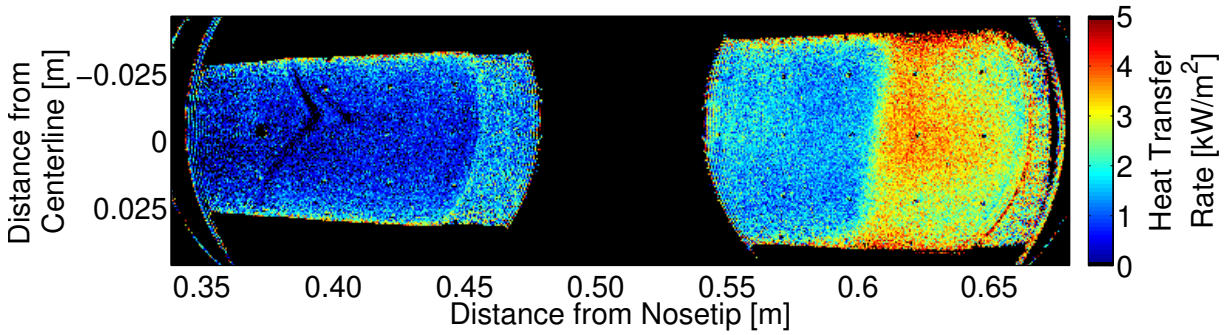

(b) $Re = 1.8 \times 10^6/\mathrm{m}$

Figure 22. Heat transfer data for smooth nosetip at two different Reynolds numbers. Flow is from left to right.

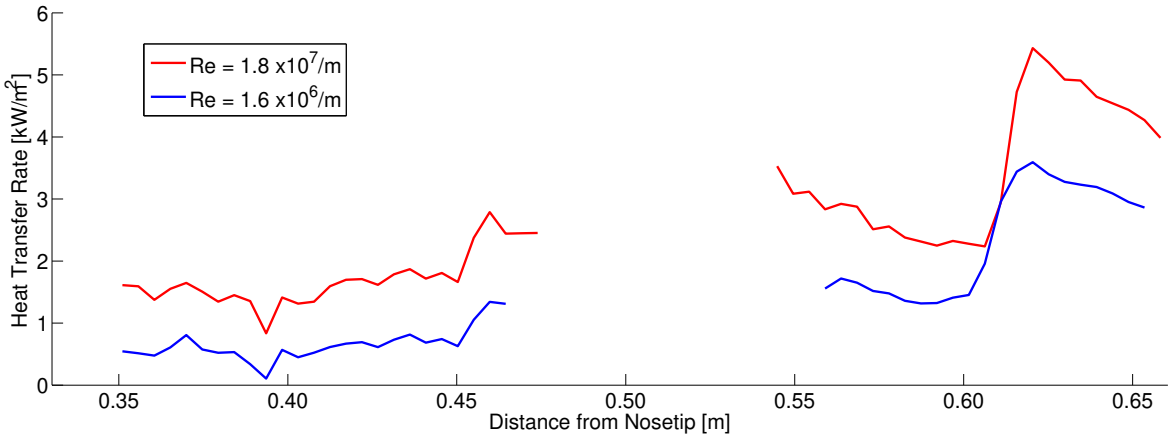

Figure 23. Heat transfer profiles for the smooth nosetip at Reynolds numbers of $1.8 \times 10^7/\mathrm{m}$ and $1.6 \times 10^7/\mathrm{m}$.

0.61 m from the nosetip. If the region of higher heating were due to transition, it would be expected to move with a change in Reynolds number. Since it does not move, it is likely that the bow shock from the blunt nosetip reflects off the wind tunnel walls and impinges on the aft end of the model.

Distributed roughness of two different RMS roughness heights was applied to the nosetip. Sandblasting the nosetip created an average RMS roughness height of 20 μm, and applying nail polish dots created an average RMS roughness height of 140 μm. Heat transfer rate images using each roughness at a Reynolds number of 1.8×10^7/m are shown in Figure 24. The images appear similar to each other, and also similar to the heat transfer image for the smooth nosetip (Figure 22(a)).

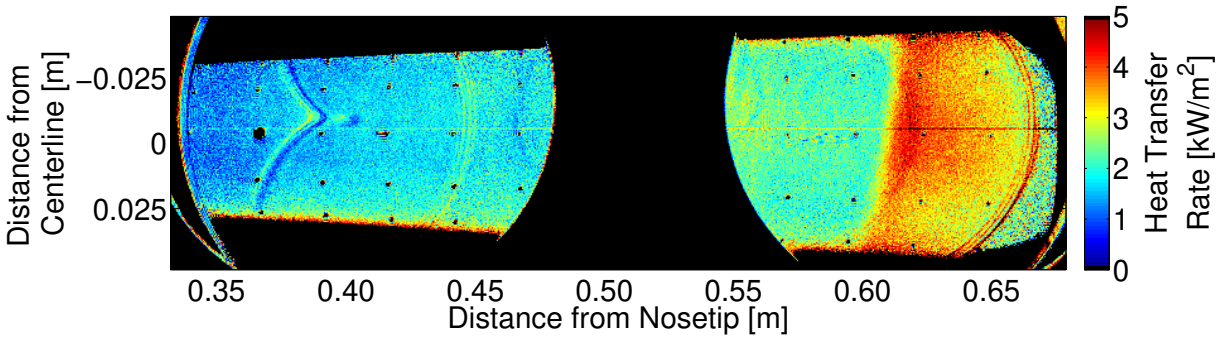

(a) 20 μm distributed roughness on nosetip.

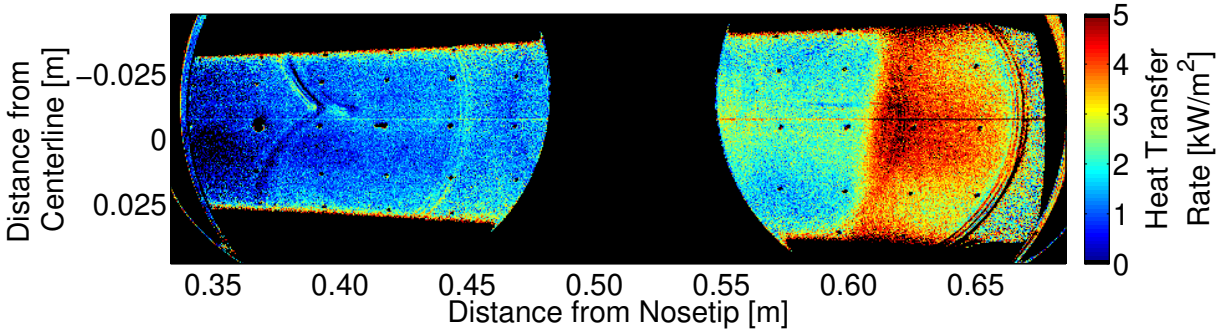

(b) 140 μm distributed roughness on nosetip.

Figure 24. Heat transfer data for different height distributed roughness on nosetip. $Re = 1.8 \times 10^7$**/m. Flow is from left to right.**

Streamwise heat transfer profiles were created for the experiments with distributed roughness and are shown in Figure 25. Although the heat transfer rate varies between the different height roughness arrays, the trend of the data is similar. Distributed roughness of the heights tested does not appear to induce transition on the model.

Isolated roughness elements 130-μm-high and 380-μm-high were also tested on the nosetip. In both cases, a region of higher heating was observed behind the roughness element. Heat transfer images for these roughness elements are shown in Figure 26. The camera was positioned closer to the nosetip of the cone for these images, so the region of higher heating due to the reflected shock is not visible. A paste-on thermocouple is seen as a dark-colored rectangle near 0.56 m from the nosetip.

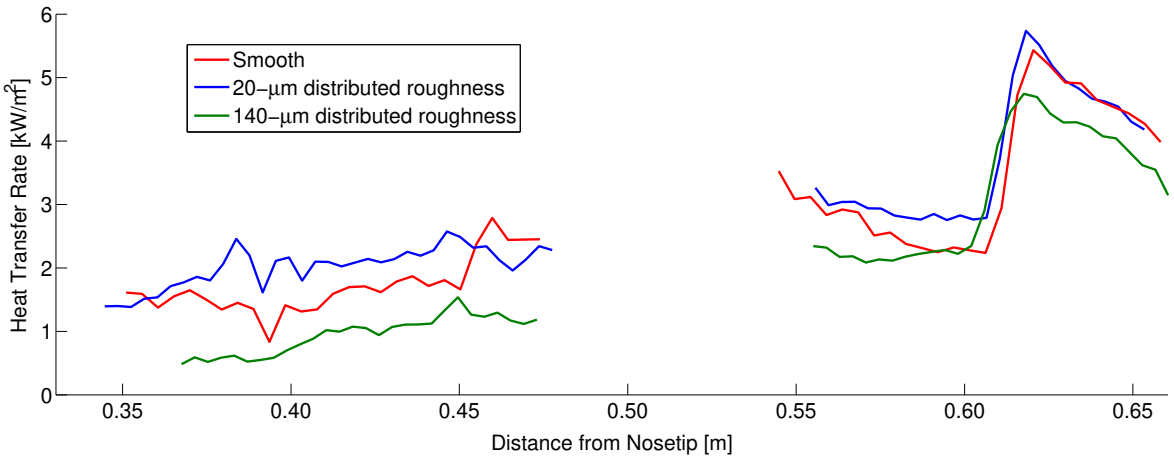

Figure 25. Heat transfer profiles comparing the smooth nosetip data to that with distributed roughness. $Re = 1.8 \times 10^7/\mathbf{m}$.

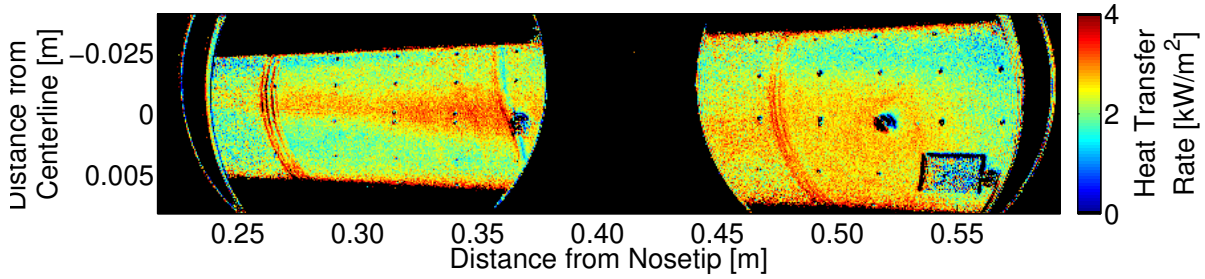

(a) 130 μm isolated roughness element on nosetip.

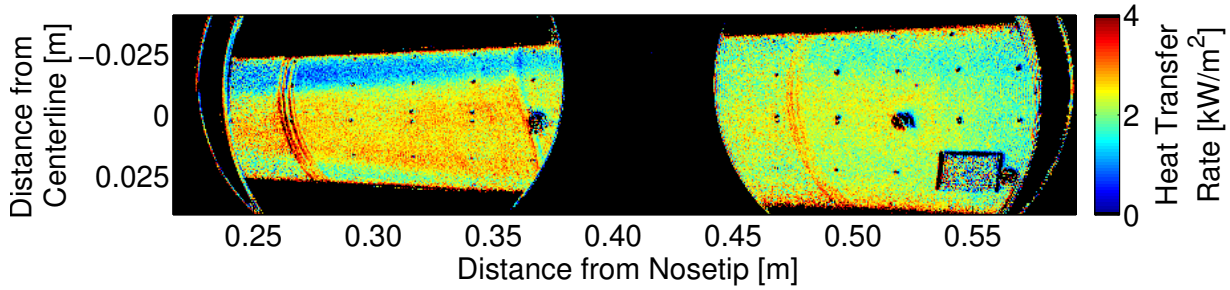

(b) 380 μm isolated roughness element on nosetip.

Figure 26. Heat transfer data for different height isolated roughness elements on nosetip. $Re = 1.8 \times 10^7/\mathbf{m}$. **Flow is from left to right.**

Spanwise heat transfer profiles were created from the images of Figure 26 by averaging 10 pixels in the streamwise direction with a moving average of 2 pixels in the spanwise direction, centered at 0.353 m from the nosetip. As the isolated roughness height was increased, the region of higher heating broadened in the spanwise direction (Figure 27). The isolated roughness elements might be causing transition within the region of higher heating.

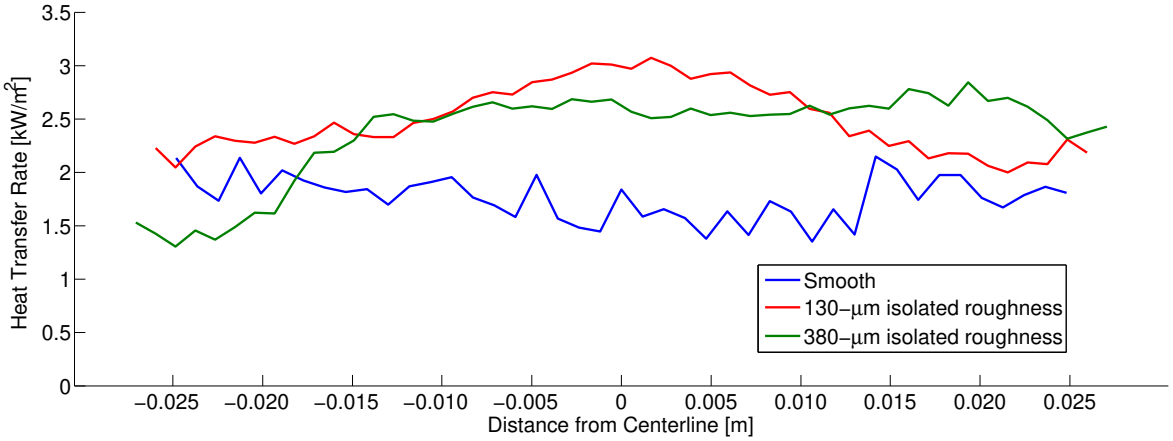

Figure 27. Heat transfer profiles at 0.353 m from the nosetip, comparing the smooth nosetip data to that with isolated roughness elements. $Re = 1.8 \times 10^7/\mathbf{m}$.

B. Summary of Blunt-Nosetip-Roughness Experiments

Several roughness configurations were tested on a blunt 3° half-angle cone, including distributed and isolated roughness elements. A region of higher heating was observed beginning near 0.61 m from the nosetip in all roughness configurations. The location of the onset of higher heating did not move with a change in Reynolds number, so the region is thought to be due to the bow shock reflecting off the tunnel walls and impinging on the model. No clear difference was visible between the smooth nosetip and the distributed roughness configurations, so distributed roughness of the heights tested do not seem to affect the flow. When using an isolated roughness element, a region of higher heating was visible behind the roughness. This region increased in spanwise width as the roughness height was increased. It is possible that transition is occurring within the region of higher heating behind the isolated roughness elements.

VIII. Conclusions

Measurements of instabilities in the wake of an isolated roughness element in the laminar nozzle-wall boundary layer of the BAM6QT are continuing. When the roughness height is nearly-critical, a new set of instabilities have been measured. Improving the repeatability is vital when attempting to select a case for comparison with computations. Future tests will look at the effect of various experimental parameters such as nozzle wall temperature on the repeatability.

Experiments were performed with a 7° half-angle cone at 0° angle of attack in order to test a method of determining heat transfer from the temperature-sensitive paint images. It was found that five of the six SB gauges yielded heat transfer that agreed well with the theory, and if one of these accurate gauges was used to calibrate the TSP, the calibrated TSP also agreed well with the theory.

A forward-facing cavity of adjustable depth was tested in the BAM6QT to determine the critical depth where self-sustaining oscillations begin. This depth was found to be approximately 1.2 cavity diameters. The measured resonant frequency at various cavity depths under both noisy and quiet flow agreed well with

the theory.

A shock tube is being constructed at Purdue to calibrate sensors, in particular the PCB-132 sensors. The shock tube is expected to be completed shortly. The tube is designed to produce clean, weak shocks with amplitudes similar to second-mode waves seen in hypersonic wind tunnels. This will allow for accurate calibrations of sensors for instability measurements.

A flared cone was tested in the BAM6QT, and showed natural transition under fully quiet flow. The streamwise vortices were seen, and followed the typical pattern of heating, cooling, reheating and then transitioning to turbulence. This was captured in a single image for the first time. The vortices were also found to be body fixed when the cone was rolled 30° in either direction.

Several different distributed and isolated roughness configurations were tested on a blunt 3° half-angle cone. A sharp rise in heat transfer was observed beginning near 0.61 m from the nosetip in all roughness configurations. The location of the onset of higher heating did not move with a change in Reynolds number, therefore the region is thought to be due to the bow shock reflecting off the tunnel walls and impinging on the model. This shock impingement obscured the effect of nosetip roughness on transition.

IX. Acknowledgements

The research is funded by AFOSR, a NASA cooperative agreement, by an NDSEG Fellowship and by the NASA Aeronautics Scholarship Program. Jerry Hahn of the Purdue AAE department machine shop did an outstanding job of manufacturing the various parts for the shock tube. Joe Jewell of Caltech provided useful drawings and photographs of the 6-inch shock tube at GALCIT. Jason Damazo also provided helpful information about the mechanisms of the 6-inch shock tube.

References

[1]Tirtey, S. C., *Characterization of a Transitional Hypersonic Boundary Layer in Wind Tunnel and Flight Conditions*, Ph.D. thesis, Von Karman Institute for Fluid Dynamics, Brussels, Belgium, August 2006.

[2]Morkovin, M. V., "Critical Evaluation of Transition from Laminar to Turbulent Shear Layers with Emphasis on Hypersonically Travelling Bodies," Air Force Flight Dynamics Laboratory Rep. AFFDL-TR-68-149, April 1969.

[3]Reed, H. L., Saric, W. S., and Arnal, D., "Linear Stability Theory Applied to Boundary Layers," *Annual Review of Fluid Mechanics*, Vol. 28, 1996, pp. 389–428.

[4]Wheaton, B. M., Juliano, T. J., Berridge, D. C., Chou, A., Gilbert, P. L., Casper, K. M., Steen, L. E., Schneider, S. P., and Johnson, H. B., "Instability and Transition Measurements in the Mach-6 Quiet Tunnel," AIAA Paper 2009-3559, June 2009.

[5]Wheaton, B. M. and Schneider, S. P., "Roughness-Induced Instability in a Laminar Boundary Layer at Mach 6," AIAA Paper 2010-1574, January 2010.

[6]Ward, C. A. C., Wheaton, B. M., Chou, A., Gilbert, P. L., Steen, L. E., and Schneider, S. P., "Boundary-Layer Transition Measurements in a Mach-6 Quiet Tunnel," AIAA Paper 2010-4721, June 2010.

[7]Chou, A., Wheaton, B. M., Ward, C. A. C., Gilbert, P. L., Steen, L. E., and Schneider, S. P., "Instability and Transition Research in a Mach-6 Quiet Tunnel," AIAA Paper 2011-283, January 2011.

[8]Wheaton, B. M., Bartkowicz, M. D., Subbareddy, P. K., Schneider, S. P., and Candler, G. V., "Roughness-Induced Instabilities at Mach 6: A Combined Experimental and Numerical Study," AIAA Paper 2011-3248, June 2011.

[9]Wheaton, B. M. and Schneider, S. P., "A Roughness-Induced Instability in a Hypersonic Laminar Boundary Layer," *AIAA Journal, to appear*, 2012.

[10]Bartkowicz, M. D., Subbareddy, P. K., and Candler, G. V., "Numerical Simulations of Roughness Induced Instability in the Purdue Mach 6 Wind Tunnel," AIAA Paper 2010-4723, June 2010.

[11]Casper, K. M., Beresh, S. J., and Schneider, S. P., "Pressure Fluctuations Beneath Turbulent Spots and Instability Wave Packets in a Hypersonic Boundary Layer," AIAA Paper 2011-372, January 2011.

[12]Harris, J. E. and Blanchard, D. K., "Computer Program for Solving Laminar, Transitional, or Turbulent Compressible Boundary-Layer Equations for Two-Dimensional and Axisymmetric Flow," NASA Technical Report TM-83207, February 1982.

[13]Schneider, S. P., Rufer, S. J., Randall, L., and Skoch, C. R., "Shakedown of the Purdue Mach-6 Quiet-Flow Ludwieg Tube," AIAA Paper 2001-0457, January 2001.

[14]Martellucci, A., Chaump, L., and Rogers, D., "Experimental Determination of the Aeroacoustic Environment about a Slender Cone," *AIAA Journal*, Vol. 11, No. 5, May 1973, pp. 634–642.

[15]Sullivan, J. P., "Extracting Heat Transfer from TSP," Personal Communication - Email, May 2010.

[16]Liu, T. and Sullivan, J., *Pressure and Temperature Sensitive Paints*, Springer, 1st ed., 2005.

[17]Ward, C., *Hypersonic Crossflow Instability and Transition on a Circular Cone at Angle of Attack*, Master's thesis, Purdue University School of Aeronautics & Astronautics, West Lafayette, IN, December 2010.

[18]Sullivan, J. P., Schneider, S. P., Liu, T., Rubal, J., Ward, C., Dussling, J., Rice, C., Foley, R., Cai, Z., Wang, B., and Woodiga, S., "Quantitative Global Heat Transfer in a Mach-6 Quiet Tunnel," Final NASA Technical Report for Cooperative Agreement NNX08AC97A, November 2011.

[19]Berridge, D. C., Chou, A., Ward, C. A., Steen, L. E., Gilbert, P. L., Juliano, T. J., Schneider, S. P., and Gronvall, J. E., "Hypersonic Boundary-Layer Transition Experiments in a Mach-6 Quiet Tunnel," AIAA Paper 2010-1061, January 2010.

[20]White, F. M., *Viscous Fluid Flow*, McGraw-Hill, 1st ed., 1974.

[21]Lemmon, E. W. and Jacobson, R. T., "Viscosity and Thermal Conductivity Equations for Nitrogen, Oxygen, Argon and Air," *International Journal of Thermophysics*, Vol. 25, No. 1, 2004, pp. 21–69.

[22]Anderson, J. D., *Computational Fluid Mechanics and Heat Transfer*, McGraw-Hill Book Company, 1st ed., 1984.

[23]Chou, A., Ward, C. A. C., Letterman, L. E., Luersen, R. P. K., Borg, M. P., and Schneider, S. P., "Transition Research with Temperature-Sensitive Paints in the Boeing/AFOSR Mach-6 Quiet Tunnel," AIAA Paper 2011-3872, June 2011.

[24]Letterman, L. E., *Instability and Transition on a Von Karman Ogive in a Mach-6 Quiet Tunnel*, Master's thesis, Purdue University School of Aeronautics & Astronautics, West Lafayette, IN, December 2011.

[25]Liu, T., Personal Communication - Email, October 2011.

[26]Huebner, L. D. and Utreja, L. R., "Mach 10 Bow-Shock Behavior of a Forward-Facing Nose Cavity," *Journal of Spacecraft and Rockets*, Vol. 30, No. 3, 1993, pp. 291–297.

[27]Ladoon, D. W., Schneider, S. P., and Schmisseur, J. D., "Physics of Resonance in a Supersonic Forward-Facing Cavity," *Journal of Spacecraft and Rockets*, Vol. 35, No. 5, Sept–Oct 1998, pp. 626–632.

[28]Juliano, T. J., Segura, R., Borg, M. P., Casper, K. M., Hannon, Jr., M. J., Wheaton, B. M., and Schneider, S. P., "Starting Issues and Forward-Facing Cavity Resonance in a Hypersonic Quiet Tunnel," AIAA Paper 2008-3735, June 2008.

[29]Engblom, W. A., Yuceil, B., Goldstein, D. B., and Dolling, D. S., "Hypersonic Forward-Facing Cavity Flow: An Experimental and Numerical Study," AIAA Paper 1995-0293, Jan 1995.

[30]Engblom, W. A., Goldstein, D. B., Ladoon, D., and Schneider, S. P., "Fluid Dynamics of Hypersonic Forward-Facing Cavity Flow," *Journal of Spacecraft and Rockets*, Vol. 34, No. 4, Jul–Aug 1997, pp. 437–444.

[31]Sarohia, V. and Back, L. H., "Experimental Investigation of Flow and Heating in a Resonance Tube," *Journal of Fluid Mechanics*, Vol. 94, 1979, pp. 649–672.

[32]Ericsson, L. E. and Reding, J. P., "Unsteady Aerodynamic Flow Field Analysis of the Space Shuttle Configuration. Part III: Unsteady Aerodynamics of Bodies with Concave Nose Geometries," Tech. Rep. LMSC-D057194, Lockheed Missiles and Space Co., Inc., April 1976, NASA citation 76N25330.

[33]Vrebalovich, T., "Resonance Tubes in a Supersonic Flow Field," Tech. Rep. TR 32-378, Jet Propulsion Laboratory, California Institute of Technology, Pasadena, CA, July 1962, NASA citation 63N13447.

[34]Liepmann, H. W. and Roshko, A., *Elements of Gasdynamics*, John Wiley & Sons, Inc., New York, 1957.

[35]Segura, R., *Oscillations in a Forward-Facing Cavity Measured using Laser-Differential Interferometry in a Hypersonic Quiet Tunnel*, Master's thesis, West Lafayette, IN, Dec 2007.

[36]Steen, L. E., *Characterization and Development of Nozzles for a Hypersonic Quiet Wind Tunnel*, Master's thesis, Purdue University School of Aeronautics & Astronautics, West Lafayette, IN, December 2010.

[37]Smith, J. A., Coles, D., Roshko, A., and Prasad, A., "A Description of the GALCIT 6" Shock Tube," Unpublished GALCIT Report FM-67-1, California Institute of Technology, June 1967.

[38]Kerlo, A.-E., "Design of a 3" Inside Diameter Shock Tube for Calibrating Instrumentation," Unpublished AAE 590 Report, Purdue University, May 2010.

[39]Fujii, K., "Experiment of Two Dimensional Roughness Effect on Hypersonic Boundary-Layer Transition," *Journal of Spacecraft and Rockets*, Vol. 43, No. 4, July–August 2006, pp. 731–738.

[40]Estorf, M., Radespiel, R., Schneider, S. P., Johnson, H., and Hein, S., "Surface-Pressure Measurements of Second-Mode Instability in Quiet Hypersonic Flow," AIAA Paper 2008-1153, January 2008.

[41]Alba, C., Casper, K., Beresh, S., and Schneider, S., "Comparison of Experimentally Measured and Computed Second-Mode Disturbances in Hypersonic Boundary-Layers," AIAA Paper 2010-897, January 2010.

[42]Berridge, D. C., Casper, K. M., Rufer, S. J., Alba, C. R., Lewis, D. R., Beresh, S. J., and Schneider, S. P., "Measurements and Computations of Second-Mode Instability Waves in Several Hypersonic Wind Tunnels," AIAA Paper 2010-5002, June 2010.

[43]Bounitch, A., Lewis, D. R., and Lafferty, J. F., "Improved Measurements of "Tunnel Noise" Pressure Fluctuations in the AEDC Hypervelocity Wind Tunnel No. 9," AIAA Paper 2011-1200, January 2011.

[44]Rufer, S. J. and Berridge, D. C., "Experimental Study of Second-Mode Instabilities on a 7-Degree Cone at Mach 6," AIAA Paper 2011-3877, June 2011.

[45]Chou, A., *Characterization of Laser-Generated Perturbations and Instability Measurements on a Flared Cone*, Master's thesis, Purdue University School of Aeronautics & Astronautics, West Lafayette, IN, October 2010.

[46]Li, F., Choudhari, M., Chang, C.-L., and White, J., "Analysis of Instabilities in Non-Axisymmetric Hypersonic Boundary Layers over Cones," AIAA 2010-4643, June 2010.

[47]Sivasubrahmanian, J. and Fasel, H. F., "Numerical Investigation of Laminar-Turbulent Transition in a Cone Boundary Layer at Mach 6," AIAA 2011-3562, June.

[48]Laible, A. C. and Fasel, H. F., "Numerical Investigation of Hypersonic Transition for a Flared and a Straight Cone at Mach 6," AIAA 2011-3565, June.

[49]Terwilliger, N., *Numerical Investigation of Boundary Layer Instability Modes on a Compression Cone at Mach 6*, Master's thesis, University of Arizona Department of Aerospace and Mechanical Engineering, Tuscon, AZ, 2011.

[50]Hunt, L. E. and Saric, W. S., "Boundary-Layer Receptivity of Three-Dimensional Roughness Arrays on a Swept-Wing," AIAA 2011-3881, June 2011.

[51]Muller, L. and Henckels, A., "Visualization of High-Speed Boundary-Layer Transition with FPA In-frared Measurement," Report IB-39113-96A04, Cologne, Germany, May 1996, Translated into English by Stephan Lehner, January 2009.

[52]Gilbert, P. and Steen, L., "Instability and Transition on the CIRA 3-Degree Blunt Cone," Unpublished AAE 520 Report, Purdue University, May 2009.